FERMILAB=THESIS-2020-34

ABSTRACT

NONLINEAR INTEGRABLE OPTICS BEAM DYNAMICS EXPERIMENT AND DIAGNOSTICS

Sebastian Szustkowski, Ph.D.
Department of Physics
Northern Illinois University, 2020
Swapan Chattopadhyay, Director

All present circular particle accelerators are built around linear focusing optics. Unavoidable nonlinear elements appear in accelerators, such as magnetic aberrations and space-charge effects, which are typically corrected using nonlinear magnets. However, these added nonlinearities degrade particle beam stability, and in most cases, the system becomes non-integrable. The Integrable Optics Test Accelerator (IOTA), at Fermi National Accelerator Laboratory (Fermilab), is a test bed to study beam dynamics in integrable lattices for both electron and proton beams, independently. This work presents experimental results of the nonlinear electron beam dynamics behavior in IOTA using an elliptical nonlinear magnet. The elliptical nonlinear magnet allows for a large betatron tune spread, allowing for a stable high-intensity beam. In a future experimental run, minimally invasive beam instrumentation is needed to study time-dependent collective instabilities, and halo formation in space-charge dominated proton beams. Traditional profile monitors are too destructive to the beam or just measure one dimension of the beam. A gas sheet can be injected perpendicular to the proton beam at an angle. By doing so, a two-dimensional, turn-by-turn, transverse profile measurement can be made, which will preserve the integrity of the beam. The development and progress of a gas sheet beam profile monitor will also be presented.

NORTHERN ILLINOIS UNIVERSITY
DE KALB, ILLINOIS

DECEMBER 2020

NONLINEAR INTEGRABLE OPTICS BEAM DYNAMICS EXPERIMENT AND DIAGNOSTICS

BY

SEBASTIAN SZUSTKOWSKI

A DISSERTATION SUBMITTED TO THE GRADUATE SCHOOL

IN PARTIAL FULFILLMENT OF THE REQUIREMENTS

FOR THE DEGREE

DOCTOR OF PHILOSOPHY

DEPARTMENT OF PHYSICS

Dissertation Director:
Swapan Chattopadhyay

ACKNOWLEDGEMENTS

In memory of Mrs. Nicole Larsen, who has guided my interest into the sciences.

First and foremost I would like to thank my advisor Swapan Chattodpadhyay for his guidance, insight, and motivation in pursuing becoming a better physicist. Next I would like to thank Alexander Valishev for help discussions in accelerator physics concepts and control room experience. Thank you to Ben T. Freemire and Darren Crawford for their tremendous help in developing the gas sheet beam profile monitor. I am grateful to Alexander Romanov and Nikita Kuklev during the experimental run and their support, as well as the shared experience while gathering data in the owl shifts. I appreciate and indebted to the Fermilab Accelerator Science and Technology team, especially to the technicians Dave Franck and Elias Lopez. Thank you to U.S. Particle Accelerator School lecturers and staff for their time and teachings, and allowing me the opportunity to take numerous courses in accelerator topics. I want to thank NIU faculty and support staff, especially Carlos Garcia and Jane Pretkelis with their administrative help. I also would like to thank my fellow physics graduate students Jeremiah Mitchell, Prudhvi Nikhil Bhattiprolu, Prudhvi Raj Varma Chintalapati, Osama Mohsen, Aakaash Narayanan, Christina Sarosiek, Ramanpreet Singh, and Wei Hou Tan for being great friends! Lastly I would like to thank my loving family and my one and only Jean Stepnowski for their unconditional support and motivation.

Fermilab is operated by the Fermi Research Alliance, LLC, under Contract No. DE-AC0207CH11359 with the US Department of Energy. This work is supported by the Office of High Energy Physics General Accelerator Research and Development (GARD) Program and NIU Accelerator Cluster Funds.

DEDICATION

To Mom and Dad.

TABLE OF CONTENTS

LIST OF TABLES

LIST OF FIGURES

Figure Page

Figure Page

CHAPTER 1

INTRODUCTION

1.1 Motivation

Present accelerators are built around linear, strong focusing components to transport and store charged particle beams [1]. Imperfections in the magnets, chromatic aberrations and Coulomb self-interactions introduce nonlinearities that result in resonances. Other multipole magnets, such as sextupoles magnets used to correct chromaticity, are intentionally added to the system, which continues to drive higher order resonances. It also may couple the motion between the two focusing planes which typically leads to chaos and loss of particle stability. In addition to external nonlinearities of accelerator components, collective instabilities from the particle beam can be predominant, which will lead to a loss in particles. The collective instabilities from the beam can be suppressed by an external damping system, but doing so will further reduce the dynamical aperture [2]. These problems can be thought of a self-feedback loop of trying to correct a not-so-linear lattice with nonlinear elements. The Integrable Optics Test Accelerator (IOTA) strives to address these problems by having the accelerator inherently be nonlinear in the first place [3]. The nonlinear lattice implements a strong focusing element as prescribed by V. Danilov and S. Nagaitsev theory [4], which has a 2D integrable nonlinear motion. Inherently the 2D integrable system removes chaotic motion and particle loss in the dynamic aperture.

The first experimental phase of testing the nonlinear magnet is to understand the nonlinear particle beam dynamics behavior in a circular accelerator, by looking at the motion in

various location of the phase space. By exploring the phase space, a demonstration that the particle motion is stable for large amplitudes of motion is sought. This is achieved by kicking an electron beam at various amplitudes. Whereas the second phase is to use proton beams, with the focus of suppressing space-charge related effects in high intensity accelerators and allowing for strong nonlinear decoherence to suppress halo formation. This can pave the way for a multi-megawatt beam power for future high energy physics experiments. Presently the Fermilab proton complex delivers 700 kW to long-baseline neutrino programs. The Deep Underground Neutrino Experiment requires 1.2 MW beam power by 2026 and 2.4 MW by 2032. The Proton Improvement Plan II aims to achieve 1.2 MW beam power, whereas to achieve 2.4 MW beam power it is proposed to replace the Booster with a new rapid-cycling synchrotron utilizing nonlinear integrable optics [5]. For the latter experiment phase, low energy proton beam diagnostic is limited in IOTA, and a diagnostic device would need to be implemented to study the halo evolution and other collective instabilities in the storage ring [3, 6]. Thus a gas sheet beam profile monitor is being developed that will measure the two dimensional transverse profile of the proton beam.

1.2 Organization Overview

This dissertation discusses aspects of the Danilov-Nagaitsev Magnet. Specifically, experimental measurements at different nonlinear focusing strength of the magnet at various phase space locations. It also explores the development and commissioning aspects of a gas sheet beam profile monitor, and future outlook. The dissertation is organized as follows. Chapter 2 covers particle accelerators and dynamics from the conventional aspect and the nonlinear Danilov-Nagaitsev dynamics. Chapter 3 explores the experimental test facilities in which the nonlinear dynamics are explored, and where the gas sheet beam profile monitor

measurements will take place. While in Chapter 4 is the experimental results using the non-linear magnet. Finally, Chapter 5 discusses the development of the gas sheet beam profile monitor and its background.

CHAPTER 2

ACCELERATORS AND PARTICLE MOTION

This chapter is an introduction to particle dynamics in storage rings. Section 2.1 briefly introduces linear accelerator physics and conventional nonlinear techniques. Section 2.2 discusses space charge effects in accelerators. Section 2.3 discusses particle dynamics of a highly nonlinear transverse focusing field element that allows for large transverse tune spread without degradation of the beam. Section 2.4 goes over the beam instrumentation and diagnostics.

2.1 Traditional Accelerators

Fundamentally all charged particle motion in an electromagnetic field, $\vec{E}$ and $\vec{B}$, obey the Lorentz force,

$$\frac{d\vec{p}}{dt} = \vec{F} = e(\vec{E} + \vec{v} \times \vec{B}), \tag{2.1}$$

where $\vec{p} = \gamma m \vec{v}$ is the momentum, $\gamma = 1/\sqrt{1 - v^2/c^2}$ is the relativistic Lorentz factor, m is the mass, $\vec{v}$ the velocity, and e is the charge. Additionally, the relationship between the electric and magnetic field with respect to the vector potential $\vec{A}$ and scalar potential Φ is given by $\vec{E} = -\nabla\Phi - \partial\vec{A}/\partial t$, and $\vec{B} = \nabla \times \vec{A}$. A general expression for the Hamiltonian, the equations of motion, and the canonical momentum for particle motion in accelerators described as in terms of the electromagnetic four-potential, [7]

$$H = c[m^2c^2 + (\vec{V} - e\vec{A})^2]^{1/2} + e\Phi, \tag{2.2}$$

$$\dot{q} = \frac{\partial H}{\partial P_q}, \qquad \dot{P}_q = -\frac{\partial H}{\partial q}, \tag{2.3}$$

$$\vec{P} = \vec{p} + e\vec{A}, \tag{2.4}$$

where q is a generalized coordinate, and overdot is the derivative with respect to time t. For cyclic motion, it is often beneficial to describe the motion in a curvilinear coordinate system. The Frenet-Serret coordinate system is then introduced. In this frame, the particles follow along a reference orbit, where s is the propagation distance along the reference orbit, depicted in Fig. 2.1. The coordinates (x, y, s) follow the curvilinear path of the beam frame along a reference orbit $\vec{r_0}$. The initial position of the particle (blue dot) in the beam frame is $x\hat{x} + y\hat{y}$, while in the lab frame it is $\vec{r} = \vec{r_0} + x\hat{x} + y\hat{y}$.

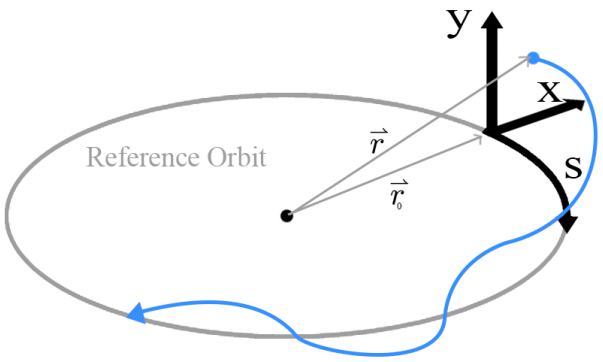

Figure 2.1: Frenet Serret coordinate system.

In this approach, s will be chosen to be the independent variable where the Hamiltonian is

$$H = -eA_s - (1 - \frac{x}{\rho})[(\frac{E - e\Phi}{c})^2 - (p_x - eA_x)^2 - (p_y - eA_y)^2 - m^2c^2]^{1/2}, \tag{2.5}$$

where ρ is the local radius of curvature of the reference orbit, and the canonical vector potentials are

$$\begin{aligned} A_x &= \hat{x} \cdot \vec{A}, \\ A_y &= \hat{y} \cdot \vec{A}, \\ A_s &= (1 + \frac{x}{\rho})\hat{s} \cdot \vec{A}. \end{aligned} \tag{2.6}$$

These equations now prescribe the general motion of a particle in a periodic accelerator for any given potential from any electromagnetic field.

2.1.1 Transverse Focusing Optics

The most simple example of an accelerator is a periodic storage ring. The particle beam is contained in the ring with alternating polarity, quadrupole magnets. The linear equation of motion in the transverse plane is described as [1]

$$\frac{d^2x}{ds^2} = -K(s)x, \tag{2.7}$$

where x is the deviation from the ideal trajectory and $K(s)$ is the quadrupole focusing coefficient, which is given by

$$K = \frac{B_T}{(B\rho)a}. \tag{2.8}$$

The quadrupole focusing coefficient is determined by the properties of the quadrupole magnet by its magnetic pole-tip field B_T, and the pole-tip radius a, as well as, the property of the design particle beam momentum p, and storage ring radius called the magnetic rigidity

$$(B\rho)[\text{T-m}] \approx 3.356p \text{ [GeV/c]}. \tag{2.9}$$

The linear equation of motion leads to the Hamiltonian

$$H = \frac{p_x^2 + p_y^2}{2} + K_x(s)\frac{x^2}{2} + K_y(s)\frac{y^2}{2}, \tag{2.10}$$

where H is an invariant of the motion. The transverse motion has two degrees of freedom the equation of motion is a linear oscillator. This leads to two invariants, which are called the action or integrable of motion. The action variable is a measurement of a single particle orbit amplitude, or equivalently the enclosed volumetric phase space, which is defined by

$$J_z = \frac{1}{2\pi}\oint p_z dz. \tag{2.11}$$

The total phase space volume occupied by a distribution of independent particles is conserved. The canonical transformation to normalized coordinates, with $z = x$ or y, is:

$$\begin{aligned} z_N &= \frac{z}{\sqrt{\beta(s)}}, \\ p_{z,N} &= p_z\sqrt{\beta(s)} + \frac{\alpha z}{\sqrt{\beta(s)}}. \end{aligned} \tag{2.12}$$

This leads to a normalized Hamiltonian

$$H = \frac{p_{x,N}^2 + p_{y,N}^2}{2} + \frac{x_N^2}{2} + \frac{y_N^2}{2}. \tag{2.13}$$

For a constant beam energy, the solution to (2.7) can be parameterized as

$$x(s) = \sqrt{2J\beta_x(s)}\cos(\phi_x(s) + \phi_0), \tag{2.14}$$

where $\beta_x(s)$ is called the beta function, which also defines the beam envelope, $\phi_x(s)$ is the phase advance, and J is the action variable. Along with the beta function, there are two more parameterizations describing the betatron motion, which are

$$\begin{aligned} \alpha(s) &= -\frac{1}{2}\frac{d\beta}{ds}, \\ \gamma(s) &= \frac{1+\alpha^2(s)}{\beta(s)}. \end{aligned} \tag{2.15}$$

The functions $\beta(s)$, $\alpha(s)$, and $\gamma(s)$ are called Courant-Snyder parameters or Twiss parameters. The action variable or also called the emittance ϵ is related to the Twiss parameters by

$$2J = \epsilon = \gamma x^2 + 2\alpha x' x + \beta x'^2. \tag{2.16}$$

Here the action is area preserving under the phase space (x, x'), and is a constant of motion. For a given beam distribution $\rho(x, x^{'})$ in the phase space $(x, x^{'})$, the first and second moments for coordinate x is described as

$$< x >= \frac{\int_0^\infty x\rho(x)dx}{\int_0^\infty \rho(x)dx} = \frac{1}{N}\sum_{i=1}^{N} x_i, \tag{2.17}$$

and

$$< x^2 >= \frac{\int_0^\infty x^2\rho(x)dx}{\int_0^\infty \rho(x)dx} = \frac{1}{N}\sum_{i=1}^{N} x_i^2. \tag{2.18}$$

Similar treatment is done for the distribution of the angle $< x^{'} >$, and its second moment $< x^{'2} >$, as well as coupling terms $< xx^{'} >$. Thus the beam matrix Σ_{beam} can be defined

relating the Twiss parameters (α, β, γ), along with the emittance ϵ to the first and second moment of the distribution for both in position x and angle $x^{'}$. This is given by

$$\Sigma^{x}_{beam} = \epsilon_x \begin{pmatrix} \beta & -\alpha \\ -\alpha & \gamma \end{pmatrix} = \begin{pmatrix} < x^2 > - < x >^2 & < xx^{'} > - < x >< x^{'} > \\ < x^{'}x > - < x^{'} >< x > & < x^{'2} >< x^{'} >^2 \end{pmatrix}. \quad (2.19)$$

The root-mean-square (RMS) of the distribution is typically a physical measurement and is defined as

$$\sigma_x = \sqrt{< x^2 > - < x >^2}, \quad (2.20)$$

where usually the mean $< x >^2$ is neglected. The other transverse phase space coordinate $(y, y^{'})$ is treated the same way for its beam matrix. Analogues to the transverse space, the longitudinal phase space is described by the RMS bunch length $\sigma_z =< z^2 >^{\frac{1}{2}}$ or in terms of RF phase $\sigma_\phi = \omega_{rf}\sigma_z/c$ and the RMS momentum spread $\sigma_\delta =< \delta^2 >^{\frac{1}{2}}$. Which makes the longitudinal 2D phase space coordinate as (ϕ, δ). The full 6D phase space $(x, x^{'}, y, y^{'}, z, \delta)$ can then be characterized with a 6×6 matrix, where if the system is uncoupled, then the Σ_{beam} is represented in block-diagonal form. The transverse and longitudinal emittance are calculated from the respective determinant of the beam matrix by $\epsilon_x = \sqrt{\det\Sigma^{x}_{beam}} = \sqrt{< x^2 >< x^{'2} > - < xx^{'} >^2}$. For the emittance to an invariant under acceleration, the normalized emittance is defined $\epsilon_N \equiv \beta\gamma\epsilon$, where β and γ are the relativistic factors.

2.1.1.1 General Transfer Matrix

The transverse dynamics of a single particle can be described by transport matrices. The trajectory of the phase space, (x, x'), can be generalized through a linear transformation from its initial location i to its final location f as

$$\begin{pmatrix} x \\ x' \end{pmatrix}_f = \begin{pmatrix} R_{11} & R_{12} \\ R_{21} & R_{22} \end{pmatrix}_{fi} \begin{pmatrix} x \\ x' \end{pmatrix}_i . \tag{2.21}$$

The general transfer matrix can be expanded to a full 6-dimension $(x, x', y, y', z, \delta)$ treatment with both transverse planes and longitudinal plane. Where the longitudinal phase space can be described as δ, the relative energy error, and z, the longitudinal distance of a co-moving frame.

The optical function can also be transported by R matrix elements from Eq. (2.21) by:

$$\begin{pmatrix} \beta \\ \alpha \\ \gamma \end{pmatrix}_f = \begin{pmatrix} R_{11}^2 & -2R_{11}R_{22} & R_{12}^2 \\ -R_{11}R_{21} & 1 + 2R_{12}R_{21} & -R_{12}R_{22} \\ R_{21}^2 & -2R_{21}R_{22} & R_{22}^2 \end{pmatrix}_{fi} \begin{pmatrix} \beta \\ \alpha \\ \gamma \end{pmatrix}_i . \tag{2.22}$$

This matrix can also express the elements of the R matrix in terms of the optical functions and the betatron phase, $\phi_{fi} = (\phi_f - \phi_i)$, advance between the two locations as:

$$\mathbf{R}_{fi} = \begin{pmatrix} \sqrt{\frac{\beta_f}{\beta_i}}(\cos\phi_{fi} + \alpha_i \sin\phi_{fi}) & \sqrt{\beta_f \beta_i}\sin\phi_{fi} \\ -\frac{1+\alpha_f\alpha_i}{\sqrt{\beta_f\beta_i}}\sin\phi_{fi} + \frac{\alpha_i - \alpha_f}{\sqrt{\beta_f\beta_i}}\cos\phi_{fi} & \sqrt{\frac{\beta_i}{\beta_f}}(\cos\phi_{fi} - \alpha_f \sin\phi_{fi}) \end{pmatrix} . \tag{2.23}$$

In storage rings, the matrix 2.23 can be simplified down to a 1-turn matrix or one turn map (OTM), expressing the transportation of the particle after a full revolution when the initial location is equal to the final location. The optical functions are periodic, $\alpha(s + C)$,

$\beta(s+C)$, and $\gamma(s+C)$, where C is the circumference of the ring, and the betatron phase advance will become the 1-turn phase advance, μ. Thus the one-turn-map is then

$$\mathbf{R}_{\text{otm}} = \begin{pmatrix} \cos\mu + \alpha\sin\mu & \beta\sin\mu \\ -\gamma\sin\mu & \cos\mu - \alpha\sin\mu \end{pmatrix}. \tag{2.24}$$

The transfer matrix for a focusing quadrupole, with a gradient $k = (\partial B/\partial x)/(B\rho$ and length l, is

$$\mathbf{R}_{\text{quad}} = \begin{pmatrix} \cos\left(l\sqrt{|k|}\right) & \sin\left(l\sqrt{|k|}\right)/\sqrt{|k|} \\ -\sqrt{|k|}\sin\left(l\sqrt{|k|}\right) & \cos\left(l\sqrt{|k|}\right) \end{pmatrix}. \tag{2.25}$$

Alternatively, taking the limit for a vanishing quadrupole length while having an integrated gradient of $K = |k|l$, the transfer matrix for a thin-lens quadrupole becomes

$$\mathbf{R}_{\text{thin-quad}} = \begin{pmatrix} 1 & 0 \\ -K & 1 \end{pmatrix}. \tag{2.26}$$

2.1.1.2 Betatron Tune and Resonance

Particles that circulate around a storage ring will oscillate around the ideal orbit. The number of betatron oscillations is defined as the betatron tune, or $\nu_{x,y}$ and in some literature $Q_{x,y}$, given by the equation:

$$\nu = \frac{\mu}{2\pi} = \frac{1}{2\pi}\oint_C \frac{ds}{\beta(s)}, \tag{2.27}$$

where the μ is the betatron phase advance over one period.

Resonance in an accelerator can lead to beam loss due to the exponential growth of the amplitude of particle oscillation. Imperfections in the lattice and nonlinear fields will act as perturbations that are synchronous with the oscillation. The relation between the horizontal and vertical tunes that satisfy resonance condition is

$$m = k_x\nu_x + k_y\nu_y, \tag{2.28}$$

where m, k_x, and k_y are integers and $|k_x| + |k_y|$ is the order of the resonance. Plotting lines of different combinations of (k_x, k_y) produce a resonance diagram, or also called a tune diagram. These diagrams are beneficial in understanding the dynamical behavior of storage rings. Due to the super-periodicity of these diagrams, the fractional part of the tune is of concern. It should also be noted in circular accelerators, sum resonance should be avoided as it can lead to beam loss due to imperfections of the lattice. Whereas difference resonance can exchange the betatron oscillations between the transverse plane. Lower order resonances have faster instability if left uncorrected, which also may have feed-down effects in higher order magnets (e.g., sextupoles, octupoles , etc.), creating a magnetic quadrupole component. Figure 2.2 is a tune diagram showing resonance lines up to fifth order according to Eq. 2.28 with different integer combination of m, k_x, and k_y. First order resonance is driven by magnetic dipole imperfections, meaning that each time the beam impasses the field error, the beam will receive a transverse kick each revolution as it passes through the field error. This increases the amplitude oscillation each turn, and the beam will eventually be lost into beam pipe. Similarly, quadruple magnets drive second order resonances, sextupoles drive third order resonances, and so forth with higher order magnets.

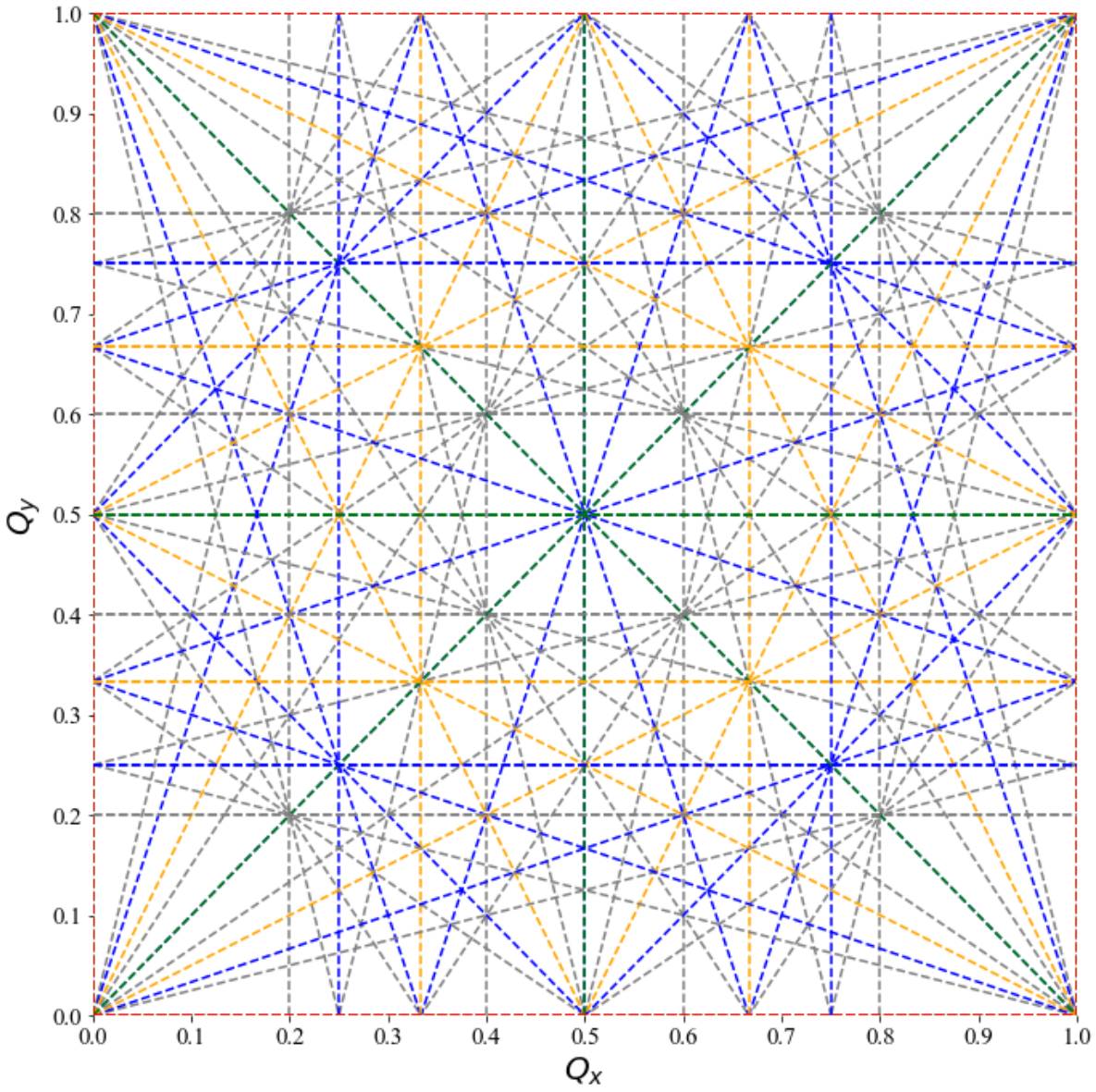

Figure 2.2: Tune diagram of up to fifth order. The color of the resonance line represents the different resonance order, where the fifth (grey), fourth (blue), third (orange), second (green), and first (red) order is shown.

2.1.1.3 Tune Shift by Quadruple Excitation

To measure the lattice beta function at a quadruple location, the quadrupole is excited. The small tune shift ($2\pi\Delta Q_{x,y} \ll 1$), that is far from the integer or half integer resonance, induced by a quadrupole excitation is then measured. For a small quadrupole excitation of ΔK, and the tune shift ΔQ induced by excitation, the beta function can be approximated as

$$\beta_{x,y} \approx \pm 4\pi \frac{\Delta Q_{x,y}}{\Delta K}. \tag{2.29}$$

2.1.1.4 Static Electric Field

Inducing an electrostatic field into an accelerator will deflect the beam according to the Lorentz force equation 2.1. Consider two conducting parallel plates separated by a distance d and applied voltage V, with a particle traversing through the length of the plated L, and then the Lorentz equation is integrated over time, the particle transverse momentum becomes $p = q\frac{V}{d}\frac{L}{\beta c}$. The particle displacement angle exiting the plates is then described as

$$\Delta\theta = \tan^{-1}\frac{p_q}{p_z} = \frac{qV}{d}\frac{L}{\beta c p_z}. \tag{2.30}$$

2.1.2 Beam Lifetime

The particle beam lifetime is important in synchrotron storage accelerators. The particle loss in the beam can be attributed to various factors, such as physical aperture, beam instabilities, collimators, scattering, etc. The main source of particle loss is due to beam gas

scattering, which is affected by elastic and inelastic scattering with electrons and nuclei of the gases, Bremsstrahlung, and ionization [8]. The lifetime for beam-gas scattering is

$$\tau_g = -\frac{1}{N}\frac{dN}{dt} = \sigma\beta cn, \tag{2.31}$$

where n is the density of the gas, βc is the speed of the particle, and σ is the total cross-section. The differential cross-section per solid angle $d\Omega = 2\pi \sin\theta d\theta$ is given by [9]

$$\frac{d\sigma}{d\Omega} = (\frac{qQ}{8\pi\epsilon_0\gamma m(\beta c)^2})^2 \frac{1}{\sin\frac{\theta}{2}^2}, \tag{2.32}$$

where q is the charge of the incoming particle, and Q is the charge of the nucleus. The scattering angle acceptance is limited by the vacuum chamber aperture and the value of the betatron function at the scattering location $\epsilon_A = A^2/\beta_A$. By taking the average value of the beta function at the scattering location, the maximum allowable scattering angle is defined as $\hat{\theta^2} = \epsilon_A / < \beta >$ [10]. Assuming small-angle scattering, the beam lifetime due to gas becomes

$$\tau_g \approx \frac{P}{\pi\beta c k_B T}(\frac{qQ}{2\pi\epsilon_0\gamma m\beta c})^2 \frac{< \beta >}{\epsilon_A}, \tag{2.33}$$

where the density of the gas molecules is expressed as $n = P/k_B T$, with k_B is Boltzmann's constant, and P and T are the gas pressure and temperature.

2.2 Space-Charge Effects

Nonlinear space-charge forces, repulsive Coulomb force in a charged particle bunch, creates a transverse tune spread. These nonlinear forces cause amplitude resonance-like growth that can lead the beam into instability. Assuming for a focusing synchrotron accelerator

lattice with equal tunes, $\nu_x = \nu_y = \nu_0$, a beam with equal transverse emittance, $\epsilon_x = \epsilon_y = \epsilon$, and uniform distributed beam with relativistic β and γ, the tune shift of incoherent betatron oscillation due to space charge is given by [11]

$$\Delta\nu = -\frac{N_t r_c}{2\pi\epsilon_N \beta\gamma^2 B_f}, \tag{2.34}$$

where N_t is the total number of particles, r_c is the classical particle radius, and B_f is the bunching factor. Which the bunching factor is defined by the ratio of the average current to the peak current. B_f has the range of $0 < B_f \leq 1$, and if $B_f = 1$ the beam is treated to be unbunched. For electrons, the classical particle radius $r_c = 2.818 \times 10^{-15}$ m, whereas for protons $r_c = 1.535 \times 10^{-18}$ m. The normalized emittance is defined as $\epsilon_N = \beta\gamma\epsilon$. This tune-shift is caused by a defocusing self-field effect, which will lead to an emittance growth and halo formation. Nominally a small fraction of particles with large transverse energy will form a halo surrounding the core of the beam, leading to degradation to the beam [12].

2.3 Nonlinear Potential

V. Danilov and S. Nagaitsev's paper [4] proposed a nonlinear accelerator lattice, which leads to integrable and stable nonlinear motion. This introduces a large betatron tune spread where bounded motion can fill a large phase space. First, to construct such a system, there needs to be an element periodicity with a drift space of equal beta functions followed by a T-insert that is an axially symmetric focusing lens. The T-insert is primarily composed of linear elements. Along the drift region, a nonlinear potential will be introduced, in which its field will satisfy Laplace's equation $\Delta V = 0$, with a new time variable $\psi' = 1/\beta(s)$. In which the new Hamiltonian can be expressed as

$$H_N = \frac{p_x^2}{2} + \frac{p_y^2}{2} + \frac{x^2}{2} + \frac{y^2}{2} + \beta(\psi)V[x_N\sqrt{\beta(\psi)}, y_N\sqrt{\beta(\psi)}, s(\psi)]. \tag{2.35}$$

The potential is then expressed as $U(x_N, y_N) = \beta(\psi)V[x_N\sqrt{\beta(\psi)}, y_N\sqrt{\beta(\psi)}, s(\psi)]$, and if the new Hamiltonian from Eq. 2.35 is time-independent, then the Hamiltonian H_N is itself an invariant of motion. The nonlinear element has a special elliptic-potential that is time-independent and satisfies Bertrand-Darboux partial differential equation given by

$$xy(U_{xx} - U_{yy}) + (y^2 - x^2 + c^2)U_{xy} + 3yU_x - 3xU_y = 0. \tag{2.36}$$

The potential is then given in terms of arbitrary functions f and g as

$$U(x, y) = \frac{f(\xi) + g(\eta)}{\eta^2 + \xi^2}. \tag{2.37}$$

Where η and ξ are expressed in Cartesian coordinates as:

$$\begin{aligned} \xi &= \frac{\sqrt{(x+c)^2 + y^2} + \sqrt{(x-c)^2 + y^2}}{2c}, \\ \eta &= \frac{\sqrt{(x+c)^2 + y^2} - \sqrt{(x-c)^2 + y^2}}{2c}. \end{aligned} \tag{2.38}$$

The second invariant of motion is expressed as:

$$I(x, y, p_x, p_y) = (xp_y - yp_x)^2 + c^2p_x^2 + 2c^2\frac{f(\xi)\eta^2 + g(\eta)\xi^2}{\xi^2 - \eta^2} \tag{2.39}$$

Which has the form of $f = \frac{f_1}{2} + f_2$ and $g = \frac{g_1}{2} + g_2$, where $f_1(\xi) = c^2\xi^2(\xi^2 - 1)$ and $g_1(\eta) = c^2\eta^2(1 - \eta^2)$. The fully integrable Hamiltonian is then

$$H(x, y, p_x, p_y) = \frac{p_x^2}{2} + \frac{p_y^2}{2} + \frac{x^2}{2} + \frac{y^2}{2} + \frac{f_2(\xi) + g_2(\eta)}{\xi^2 - \eta^2}. \tag{2.40}$$

To be physically realizable into an accelerator Laplace's equation $\Delta U = 0$ must be met, where the fields are generated by magnets external to the beam pipe. The functions f and g have the form

$$\begin{aligned} f_2(\xi) &= \xi\sqrt{\xi^2 - 1}[d + t\ \mathrm{acosh}(\xi)], \\ g_2(\eta) &= \eta\sqrt{1 - \eta^2}[b + t\ \mathrm{acos}(\eta)]. \end{aligned} \tag{2.41}$$

Arbitrary constants are b, c, d, and t. In order to have the lowest multipole expansion term to be a quadrupole, $d = 0$ and $b = \frac{\pi}{2}t$. The constant t is then the nonlinear potential strength. It can be seen in Fig. 2.3 the phase space trajectories (x, y, p_x), (x, y), (x, p_x), and (y, p_y) of single particle motion from the nonlinear element.

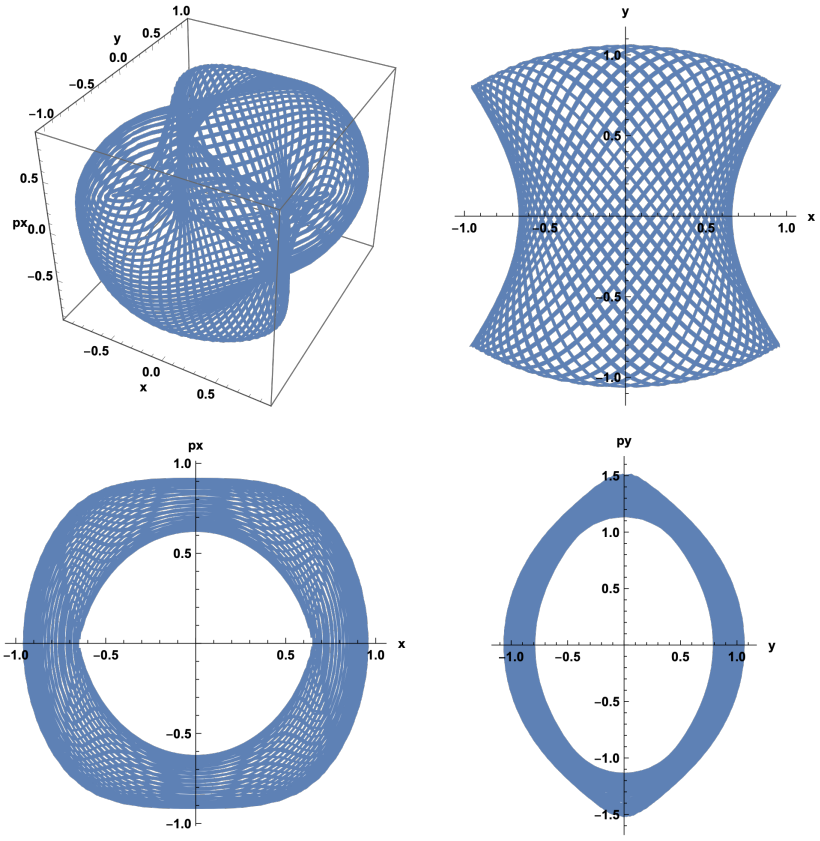

Figure 2.3: Nonlinear phase space trajectories. Starting from upper left phase space diagram and going clockwise are the phase space trajectories $(x,\, y,\, p_x)$, $(x,\, y)$, $(y,\, p_y)$, and $(x,\, p_x)$ of single particle motion

In order to determine the maximum attainable betatron tune spread at small amplitudes, a multipole expansion of the potential can be done. Thus, the small amplitude betatron tune can then be expressed as [13]:

$$\begin{aligned} Q_x &= Q_0\sqrt{1+2t}, \\ Q_y &= Q_0\sqrt{1-2t}, \end{aligned} \tag{2.42}$$

where Q_0 is the unperturbed, linear-motion, working point tune. Thus for small amplitude, stable linear motion, the range of strength values needs to be $-0.5 < t < 0.5$. There are regions of the phase space that exhibit bounded nonlinear motion for larger t values as well[14].

2.3.1 Nonlinear Potential Topology

The nonlinear potential exhibit numerous topological changes based on the varying t-strength parameter. The regions of interest in the study are $0 < t < 0.5$, where there is one stable fixed point at the origin and $0.5 < t < 0.9$, where there are two stable fixed points away from the origin. This is shown in Fig. 2.4 with varying potential strengths.

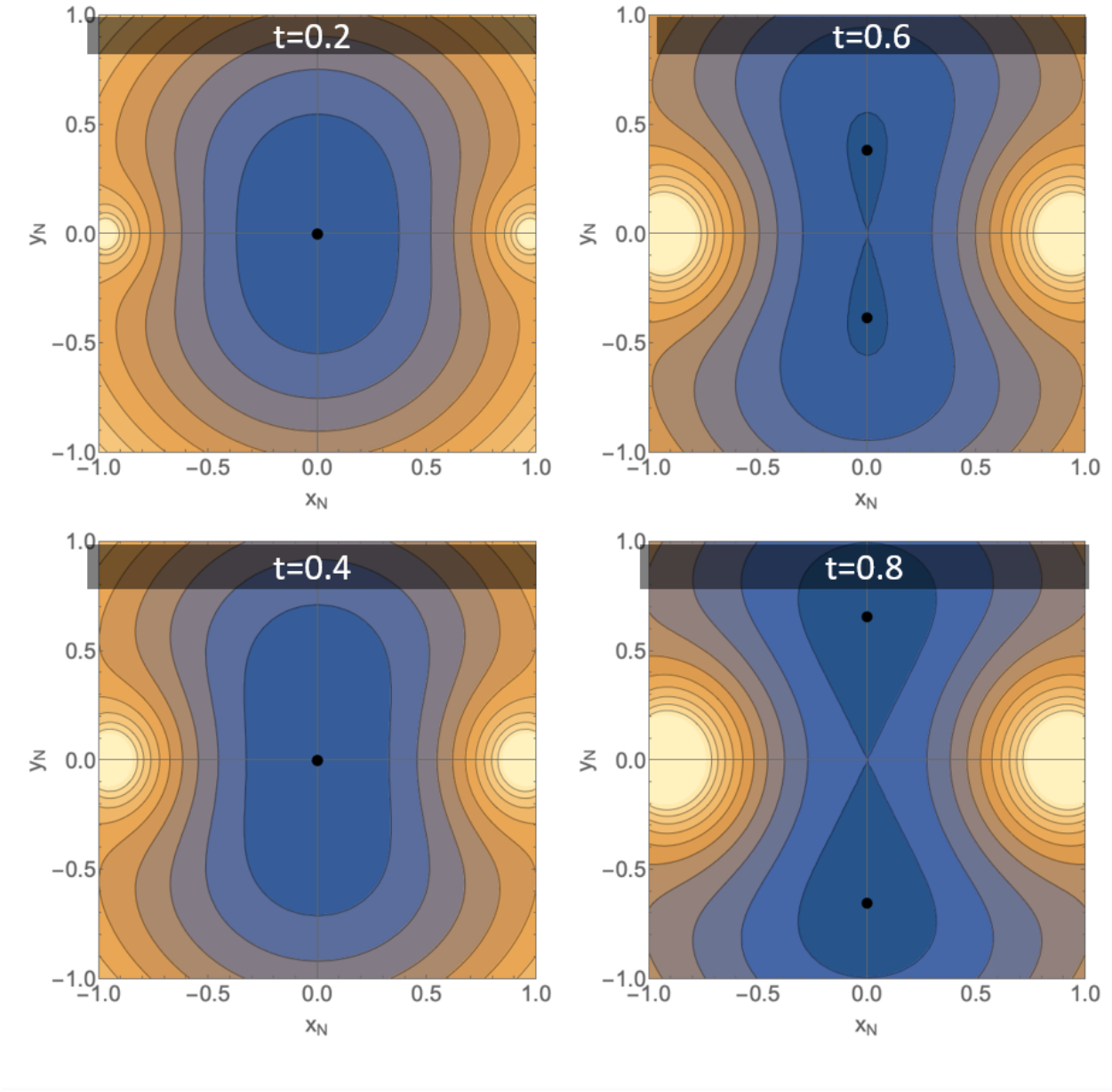

Figure 2.4: Nonlinear Potential Contours for nonlinear t-strength of 0.2, 0.4, 0.6, 0.8.

The consequence of having the the potential strength of $t > 0.5$ is that there are two circulating beams. The distance between these two stable fixed points drifts from each other as the nonlinear t-strength parameter increases. The normalized nonlinear potential from Eq. (2.40) can be expressed as [14] given by ($z = x + iy$) and the normalized nonlinear potential strength, t, as:

$$\begin{aligned} V(x,y) &= \frac{1}{2}(x^2+y^2) - tU(x,y), \\ U(x,y) &= \Re(\frac{z}{\sqrt{1-x^2}}\arcsin z). \end{aligned} \tag{2.43}$$

It can be inferred that the two stable fixed points distance increase as the square root of the nonlinear strength in the region of $0.5 < t < 0.9$. Using Mathematica [15], the distance between the two points is determined, along with a fit function of the model. The fit of the model is expressed as:

$$D = 2.385\sqrt{t-0.5}. \tag{2.44}$$

This equation is demonstrated in Fig. 2.5 where it is shown the distance between the two stable fixed points with increasing the nonlinear strength. THe black point denotes zero potential.

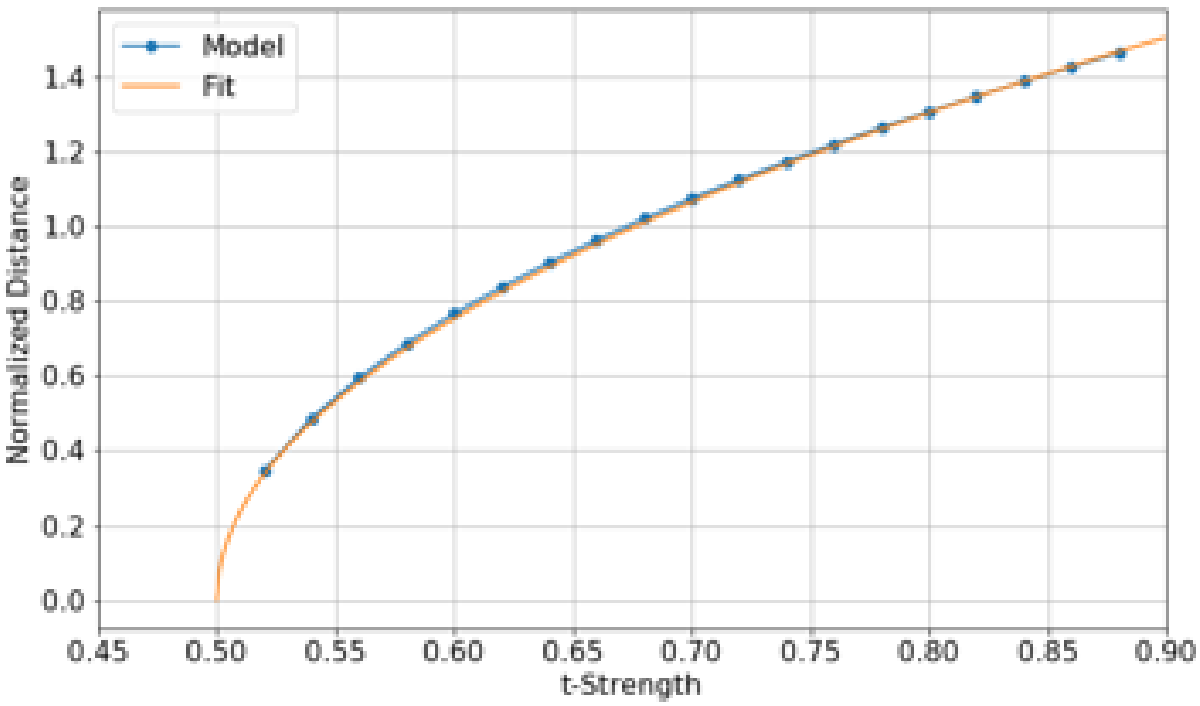

Figure 2.5: Stable Fixed Fixed Points Distance With Varying Potential Strength.

2.4 Beam Measurements

The tools for electron beam measurements in IOTA used in this dissertation were beam position monitors (BPMs), synchrotron light monitors, toroids and wall current monitors. Lastly, a gas ionization monitor being developed for proton beam mode, measures the two-dimensional transverse profile is covered extensively in Chapter 5. The beam position monitors measures the centroid of the beam, turn-by-turn, via capacitive plates in the vertical and horizontal plane. Recorded displacement of the beam by a kick gives the fractional part of the tune, via a Fast Fourier Transform, for its respective plane. This is useful for studies of nonlinear detuning in the ring. Synchrotron light monitors are profile measurements of electrons in the ring, by imaging synchrotron radiation emitted from the dipole magnets. This diagnostic is particularly useful for understanding beam dynamics at integer resonance, and the topology of high nonlinear potential discussed in Section 2.3. The toriods and wall current monitors provide beam intensity measurements.

CHAPTER 3

EXPERIMENTAL TEST FACILITIES

There are two primary experimental test facilities in which experimental results in this dissertation was performed. The Danilov-Nagaitsev Nonlinear Magnet aspect is performed at Fermi National Accelerator (Fermilab) in Batavia, IL. The construction and various tests of the gas sheet beam profile monitor were performed at Fermilab, and an experimental proposal beam-based measurements at Crocker Nuclear Laboratory, in Davis, CA. An overview of these two facilities will be presented in this chapter.

IOTA was funded, designed, constructed, and operated with an R&D path towards enabling high power, high intensity neutrino science research in the future in mind, along with being a test bed to understand the idea of nonlinear integrable optics. The high intensity neutrino program is in support of the Deep Underground Neutrino Experiment (DUNE) at Fermilab depends on multi-megawatt beams. This poses a technical challenge in high energy, high intensity proton beams with space-charge forces being an effect. Space-charge forces induce rapid phase-space diffusion that leads to halo formation, beam blow-up, and losses. By imposing a designed nonlinearities in the dynamics of the beam space-charge effect is mitigated. Mitigation of space-charge leads towards a multi-megawatt beam power [16].

3.1 Fermilab Accelerator Science and Technology (FAST) facility

The Fermilab Accelerator Science and Technology (FAST) facility is a facility that works on R&D for future accelerators. Two primary particle beam sources FAST houses are the

300 MeV electron LINAC and a 2.5 MeV proton source. FAST primary focus is its circular storage ring, the Integrable Optics Test Accelerator (IOTA), which will accept either the electron or proton beam. IOTA's primary focus is integrable optics to compensate space-charge dominated proton beams.

3.1.1 IOTA

The electron injector for IOTA is the FAST LINAC, which comprises of a 5 MeV electron RF photoinjector, followed by a 25 meter long low energy beamline ($\leq$ 50 MeV), and a 100 meter long high energy ($\leq$ 300 MeV) beamline. In the low energy beamline there are two 9-cell, 1.3 GHz, capture cavities accelerating the electrons to 50 MeV. To achieve a beam energy of up to 300 MeV, the electrons are accelerated through eight 9-cell cavities in an SRF crymodule. A Lambertson magnet followed by a stripline kicker injects the beam from the FAST line into IOTA. Table 3.1 is the electron beam parameters in IOTA.

Table 3.1: Summary of IOTA Electron Beam Parameters

PARAMETER	**VALUE**
Beam Energy	150 MeV
Circumference, C_0	39.97 m
Revolution period, T_0	133.3 ns
Betatron tunes Q_x, Q_y	4-6
Average beam current	2.4 mA
RF voltage, frequency, revolution harmonic	1 kV, 30 MHz, 4
Synchrotron tune, Q_s	5.3×10^{-4}

In order to record the position of the beam in IOTA, 21 beam position monitors (BPM) are placed around the ring. Each BPM records the horizontal and vertical position with a resolution of $\leq$ 50 μm for a single 3 nC bunch, as well as a relative intensity measurement down to $\sim$50 pC/bunch. Other beam intensity measurements, include wall current monitors

(WCM) and direct current current transformer (DCCT), providing bunch-by-bunch intensity [3]. The DCCT readback is a 15 Hz average signal, with a resolution of 10 μA rms [17].

The stripline kickers in IOTA can also be used for experimental purposes as well. The beam is displaced or kicked, by creating a uniform electric field along the beam path and its respective orientation. The strength of the kicker [18] is

$$\alpha = \frac{2VL}{r}\frac{4}{\pi}\sin\frac{\theta}{2}, \tag{3.1}$$

where V is the applied voltage, L is the length of the kicker, r is the plate inner radius, and θ is the opening angle. The parameters of the vertical and horizontal kicker are listed in Table 3.2.

Located on top of each of eight (four 30° and four 60°) bending dipole magnets are synchrotron radiation beam diagnostics. The synchrotron radiation is in the visible spectrum, where it travels through a window at the end of the vacuum corner, it is then transported through an optical periscope, and then a low-noise CMOS camera that is contained in a light-tight box. The image capture rate is 10 frames per second with a resolution of 7 μm [19].

Table 3.2: Parameters of Vertical (Horizontal) Kicker

PARAMETER	**VALUE**
Plate inner radius	20 mm
Plate thickness	6 mm
Plate opening angle	65 deg
Length of plates	1050(580) mm
Maximum plate voltage	25 kV
Maximum kick angle	16(8) mrad

Figure 3.1 is a sketch of the IOTA ring. This shows the layout of various conventional accelerator components in a storage ring. Not shown is the location of the nonlinear inte-

grable optics magnet, which is placed in the drift region in the upper corners. Where in the left corner is the Quasi-Integrable Optics magnet, and the right corner is the Danilov-Nagaitsev Nonlinear Magnet. Figure 3.2 contains the lattice parameters ($\beta_{x,y}$, D_x) for the IOTA ring. The injection point is at $s = 0$ m. At $s = 5$ m and $s = 33$ m drift regions are where the nonlinear integrable optics experiments are placed. The total perimeter of IOTA is 39.97 m. Where the former location is the placement of the Danilov-Nagaitsev Nonlinear Magnet and the latter is the placement of the Quasi-Integrable Optics Octupole channel experiment. These regions are dispersion free regions, $D_x = 0$. The IOTA lattice parameters were produced with MAD-X [20].

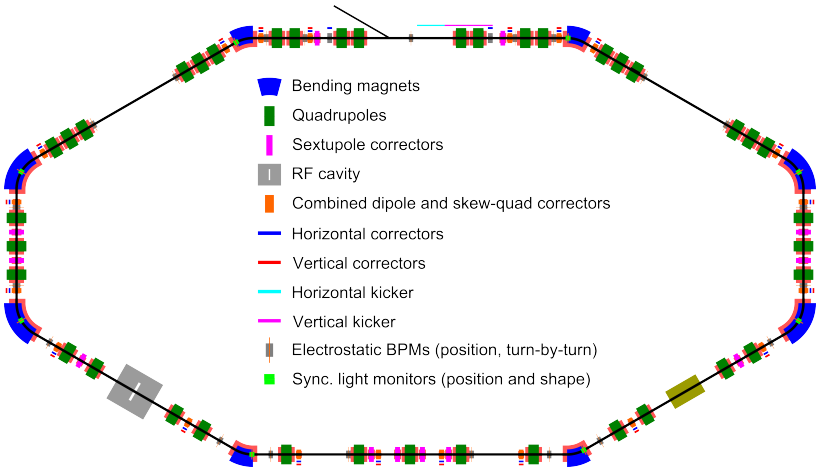

Figure 3.1: The IOTA ring layout, with the labeling of conventional accelerator components.

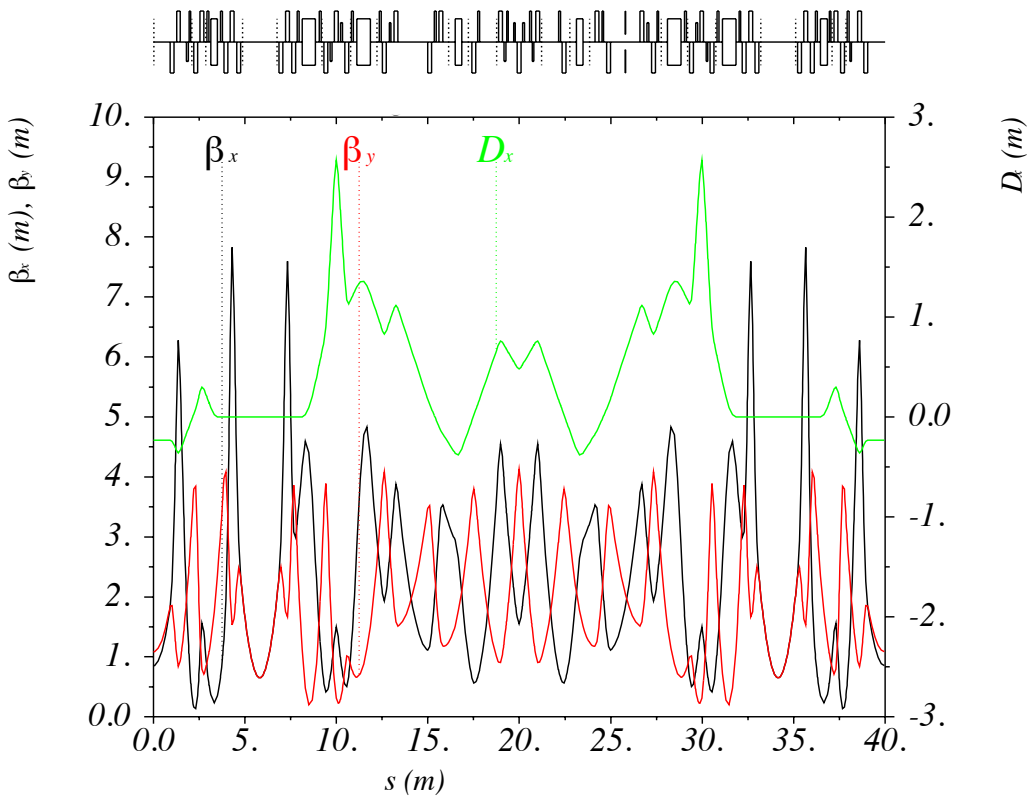

Figure 3.2: The IOTA ring lattice β-function parameters (β_x-black, β_y-red) and horizontal dispersion D_x.

3.1.1.1 Danilov-Nagaitsev Nonlinear Magnet

The nonlinear magnet and vacuum chamber were designed and manufactured by Radia-Beam Technologies. Due to the complexity of having a varying aperture, there are eighteen individual magnets that scale as the square root of β-function along the beam path. All eighteen magnets were required to have a 50 μm alignment of the magnetic axes. Each element magnetic field is also required to be within one percent of the theoretical model [21]. Figure 3.3 is a transverse view of the Danilov-Nagaitsev Nonlinear Magnet. This shows the non-conventional elliptic shape bore of the magnet.

Figure 3.3: Photograph of the Danilov-Nagaitsev Nonlinear Magnet. Used with permission by the photographer. Photo credit: Giulio Stancari.

The magnetic centers of each of the 18 magnets were aligned to ± 50 μm using a stretch copper-beryllium wire [22]. To verify the alignment of the nonlinear elements, beam based orbit response measurements were done as seen in Fig. 3.4. The alignment of the nonlinear magnet was good up to 100 μm.

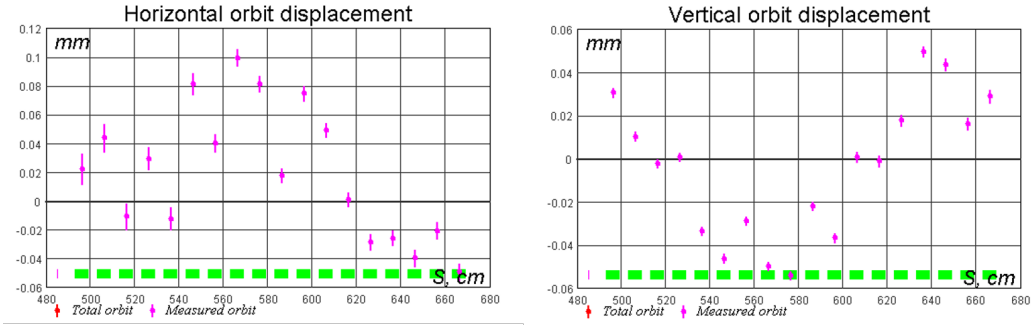

Figure 3.4: Nonlinear magnet orbit response measurement.

Since at small amplitude kicks produce a quadrupole tune response, Eq. 2.29 is used to determined the nonlinear magnet current profile. Each of the 18 magnets has to have a different current that follows along the β-function in order to create an integrable optics. Figure 3.5 demonstrates the distribution of the applied nonlinear current based off of its quadrupole component.

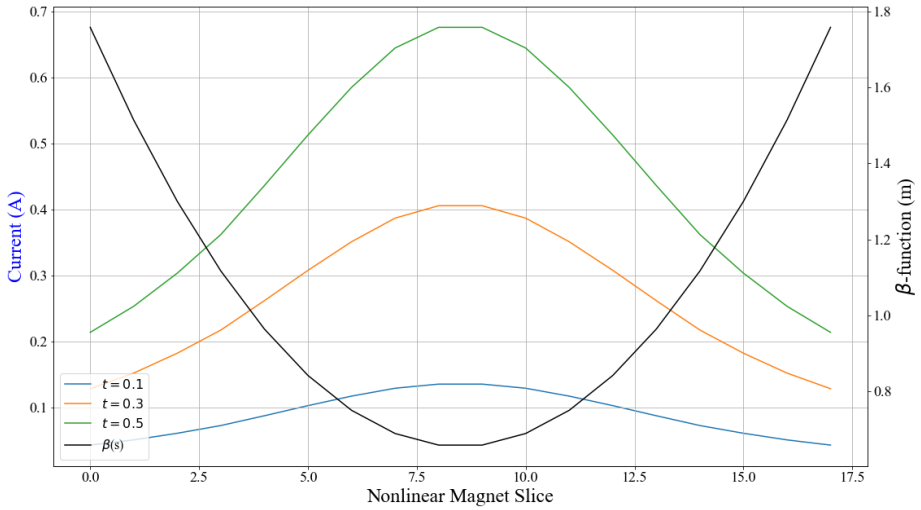

Figure 3.5: Nonlinear Magnet Current distribution for nonlinear t-strength of $t = 0.1, 0.3, 0.5$, and the lattice β-function for each magnet slice.

3.1.1.2 Proton Injector

The source of IOTA proton beam is from the previously existing HINS (High Intensity Neutrino Source) RFQ. The beam energy is 2.5 MeV and bunched at 325 MHz [23]. The low energy proton bunches will spread out and longitudinally decoheres after a few turns due to the momentum spread and nonlinearities. IOTA's RF cavity will be used to bunch the beam at 2.18 MHz. Table 3.3 provides a summary of HINS and IOTA main parameters.

Table 3.3: Summary of IOTA Proton Beam Parameters

PARAMETER	**VALUE**
Kinetic Energy	2.5 MeV
dp/p	0.1 %
Circumference, C_0	39.97 m
Revolution period, T_0	1.83 μs
RF bunching	2.18 MHz
Average beam current	8 mA
Vacuum	$6 * 10^{-10}$ Torr
Beam lifetime	300 s
Pulse rate	<1 Hz
Pulse width	1.77 μs

3.2 Crocker Nuclear Laboratory

The Crocker Nuclear Laboratory, at the University of California - Davis, houses a 76-inch isochronous cyclotron. A few applications in which users use the facility are: studying radiation effects of electronic devices in space, treatment of ocular melanoma, and nuclear physics. For the purpose of experimental measurements, the proton beam is used to ionize a gas sheet in the gas sheet beam profile monitor.

The Crocker Nuclear Laboratory cyclotron produces a beam energy range of 10.7 to 67.5 MeV. The beam energy can be further reduced by placing a Tantalum (Ta) foil of a thickness range of 72.6 to 6.35 μm. Furthermore, after the beam passes through the Ta foil, it passes through a secondary electron emission monitor (SEEM), the thickness of 101.6 μm, made out of the Aluminum (Al) foils, and then exiting out of a Kapton foil of thickness 127 μm. The reported max energy, in Table 3.4, produced by the cyclotron, is after the Kapton foil. Changing the cyclotron energy and thickness of the Ta foil, lower energies can be obtained [24].

Table 3.4: Crocker Nuclear Laboratory Beam Parameters.

Particle	Protons	Deuterons	Alphas
Max Energy (MeV)	66.6	40	60
Max Current (μA)	0.100	0.100	0.100
Max Flux ($\frac{\text{protons}}{\text{cm}^2\text{-sec}}$)	1.6E10	1.6E10	8E9

CHAPTER 4

NONLINEAR DYNAMICS MEASUREMENTS IN IOTA

The Danilov-Nagaitsev Nonlinear Magnet seeks to introduce a large betatron tune spread in which bounded particle motion can fill a large phase space. A practical realization of the magnet has been implemented into a conventional accelerator called the Integrable Optics Test Accelerator (IOTA). Experimental demonstration of large betatron tune spread is discussed. The beam stability at various nonlinear potential strength is discussed, along with stability at integer resonance.

4.1 Experimental Run

The FAST LINAC injected a 100 MeV electron beam with 4 mA of beam current circulating in IOTA. The RMS emittance was reported to be 25.3 nm in a coupled lattice and 96.3 nm uncoupled. This corresponds to an RMS beam size of 0.13 mm and 0.25 mm at the center of the nonlinear magnet, respectively. The beam condition was chosen to operate with nonlinear decoherence in the lattice [25]. After establishing a stable beam at a working point of $Q_{x,y} = 0.30$, integer tune of 5, the nonlinear magnet is turned on. Then various nonlinear strength values were explored. The beam is then kicked to various vertical amplitudes using a stripline kicker[18]. This would trigger an event in which the twenty-one beam position monitors (BPM) will start to record turn-by-turn data for 2000 turns in run one and 8000 turns in round two, and the beam intensity. The experimental measurements had two runs, with the first experimental run in the Spring of 2019 and the second experimental run in

the Spring of 2020. Measurements from the first experimental run were limited by a 6 mm aperture restriction in the AR drift section, which was fixed for the second experimental run. The other differences from the first and second run was the ability to kick the beam horizontally and in tandem with the vertical kicker. Another set pair of sextupole magnets were added as well for chromaticity correction. Figure 4.1 is a single beam position monitor (BPM) readout of the beam's vertical (orange) and horizontal (blue) position and intensity (green) signal. The BPM system records the position of the beam for 8000 turns, where the first 172 turns are background data before a kick is applied (red line). In this case, for the figure, the nonlinear strength was $t = 0.146$, and the beam decoherence in 1000 turns. The data collected from BPM's uses a python wrapper to communicate with ACNET [26] and was later formulated an automated control system [27].

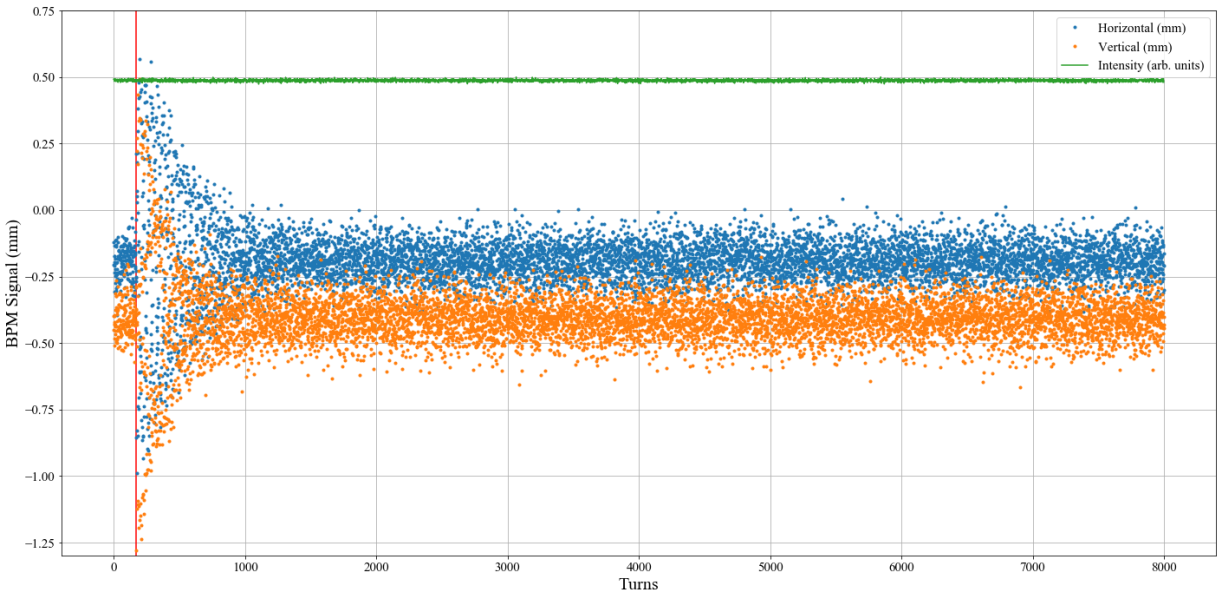

Figure 4.1: Single Beam Position Monitor vertical, horizontal, and intensity signals.

4.1.1 Results

The tune was obtained via Fast Fourier transform (FFT) from all BPM's. However, due to fast nonlinear decoherence[28], up to the first 512 turns of the data was used. To reduce uncertainty, an interpolated FFT is applied for each individual BPM signal; this allows for uncertainty in the tune measurements down to ± 0.001. An example of the FFT signal is shown in Fig. 4.2, with a nonlinear strength of $t = 0.146$. The measured tune is then compared to a lattice model. Then a 6 mm aperture restriction, in a 2 m straight section of IOTA, was applied to the model. Using MAD-X, single particle tracking is done with the models at various amplitudes and their tunes were calculated.

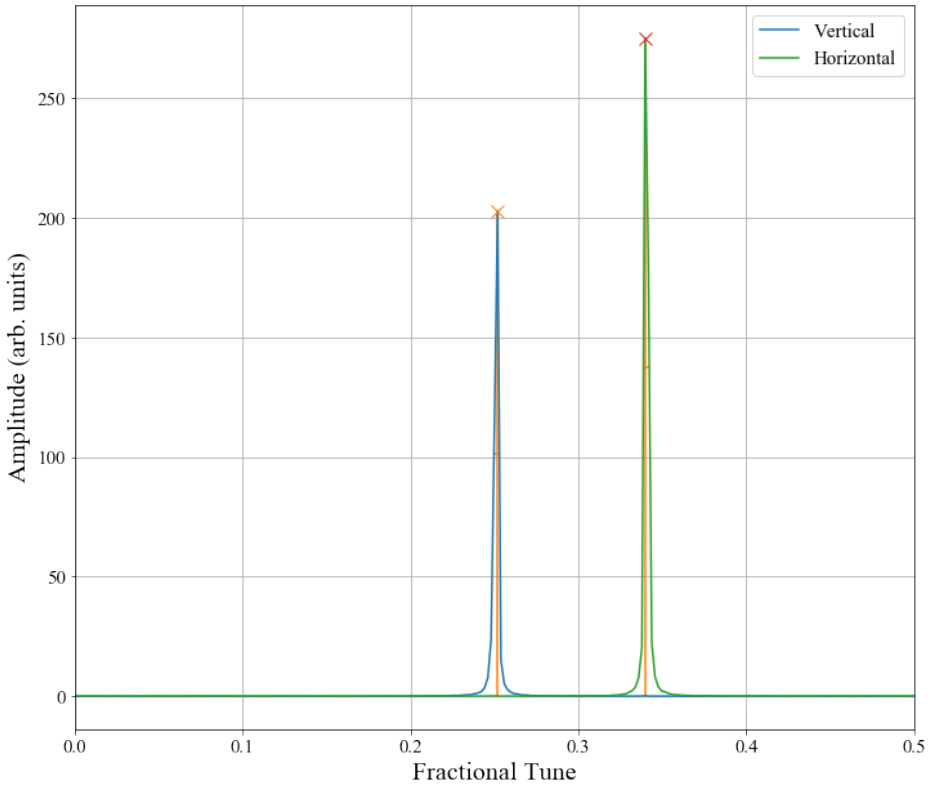

Figure 4.2: FFT spectrum for horizontal (green) and vertical (blue) signal.

4.1.1.1 Small-Amplitude Tune

Parameterizations of Eq. (2.42), the tune diagram can be explored with varying nonlinear strength parameter t, for small amplitude kicks. These small amplitude kick's strongest contributing factor is from the quadruple component from the magnets. This is shown in Fig. 4.3, where also the explored nonlinear strength values measured at a small amplitude are compared with the corresponding theoretical point. The nonlinear t-strength values shown in the figure are 0.22, 0.29, 0.36, 0.43, 0.49. The orange line is the parameterizations of Eq. (2.42), with the cyan point being the theoretical tune for its respective t-strength. The black point represents the lattice working point of $Q_{x,y} = 0.30$, integer part of the tune of 5, and green being the maximum limit given by Eq. (2.42). Red points are data points from the first experimental run, and the blue data points are from the second experimental run. The resonance lines plotted are of up to fourth order.

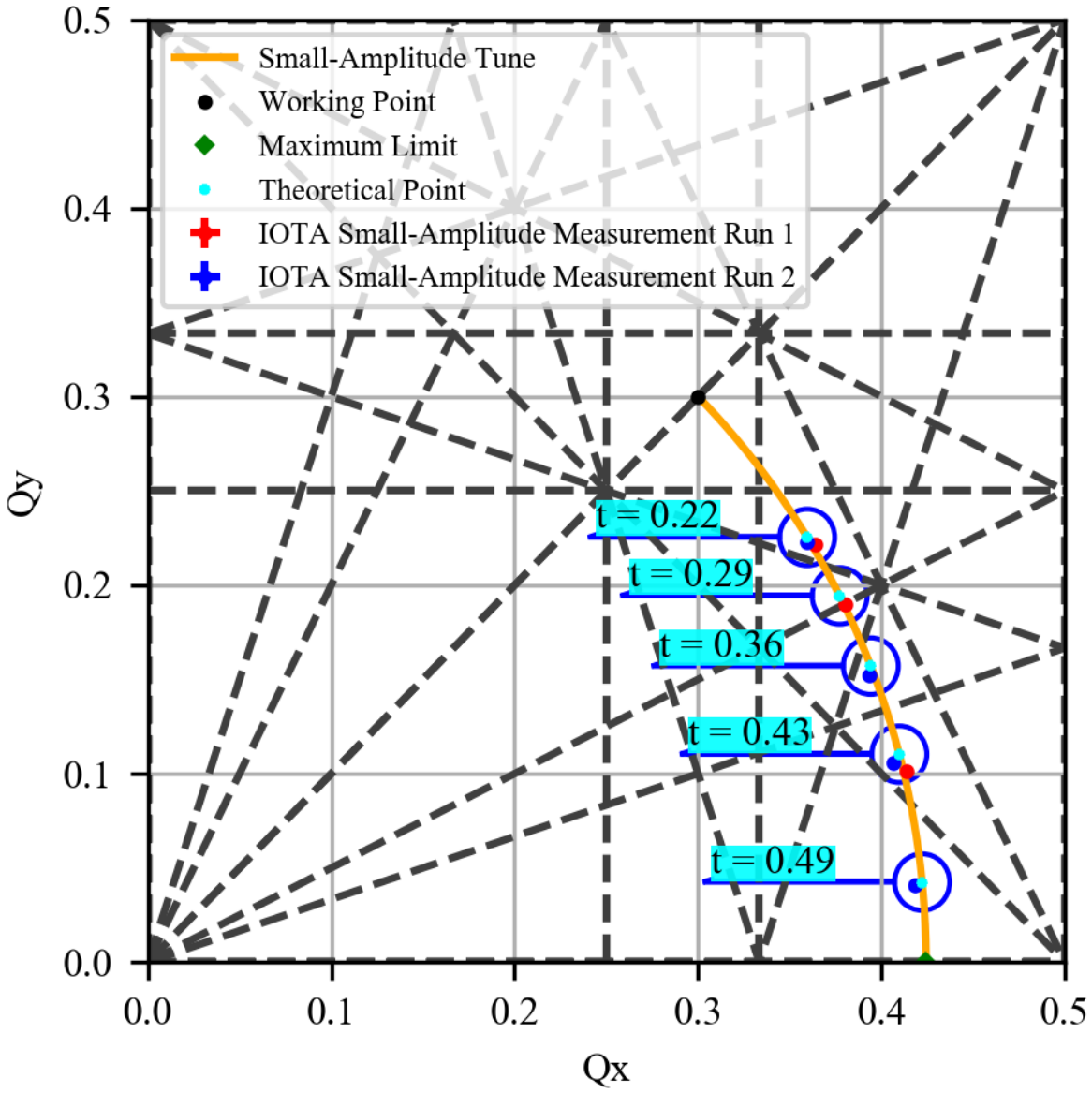

Figure 4.3: Small amplitude tune diagram of measured and theoretical tunes for nonlinear strength of $t = 0.22, 0.29, 0.36, 0.43, 0.49$.

The corresponding values from Fig. 4.3 are listed in Table 4.1. At small amplitude kicks, the tune during run one at a nonlinear strength value of $t = 0.22$ is within 2.00% of the theoretical values. Whereas at $t = 0.29$ is within 2.37% and at $t = 0.43$ is within 8.51% of the theoretical values in Eq. (2.42). Whereas during the second experimental run the nonlinear strength value of $t = 0.22$ is within 0.90%, at $t = 0.36$ is within 4.61%, at $t = 0.43$ is within 6.67%, and at the highest t-strength of $t = 0.49$ is within 2.44% of the theoretical values. The discrepancy from measured values to the theoretical values is that the theoretical values are based off of small infinitesimal amplitudes [29].

Table 4.1: Small Amplitude Tune Measurements

Parameter	Q_x	Q_y
t = 0.22		
Model	0.360	0.224
Run 1 Measurements	0.363±0.001	0.221±0.001
Run 2 Measurements	0.359±0.001	0.222±0.001
t = 0.29		
Model	0.377	0.194
Run 1 Measurements	0.380±0.001	0.190±0.001
t = 0.36		
Model	0.393	0.159
Run 2 Measurements	0.393±0.001	0.152±0.001
t = 0.43		
Model	0.409	0.112
Run 1 Measurements	0.414±0.001	0.101±0.001
Run 2 Measurements	0.406±0.001	0.105±0.002
t = 0.49		
Model	0.422	0.042
Run 2 Measurements	0.418±0.002	0.041±0.001

4.1.1.2 Beam Resonance Stability

As discussed previously, the lattice tune shifts with increasing the nonlinear t-strength. This can be visualized by following the orange line in Fig. 4.3. By increasing the nonlinear

$t-$strength the beam crosses various resonances, including the integer resonance at $Q_x = 0.4242$, $Q_y = 0$. Which at integer the nonlinear t-strength is at $t = 0.5$. Using the DCCT to record the beam current and power supply read back for the nonlinear magnet, the beam current can be diagnostic through these resonance crossing. Figure 4.4 demonstrates how the beam current and nonlinear magnet t-strength is evolved through time.

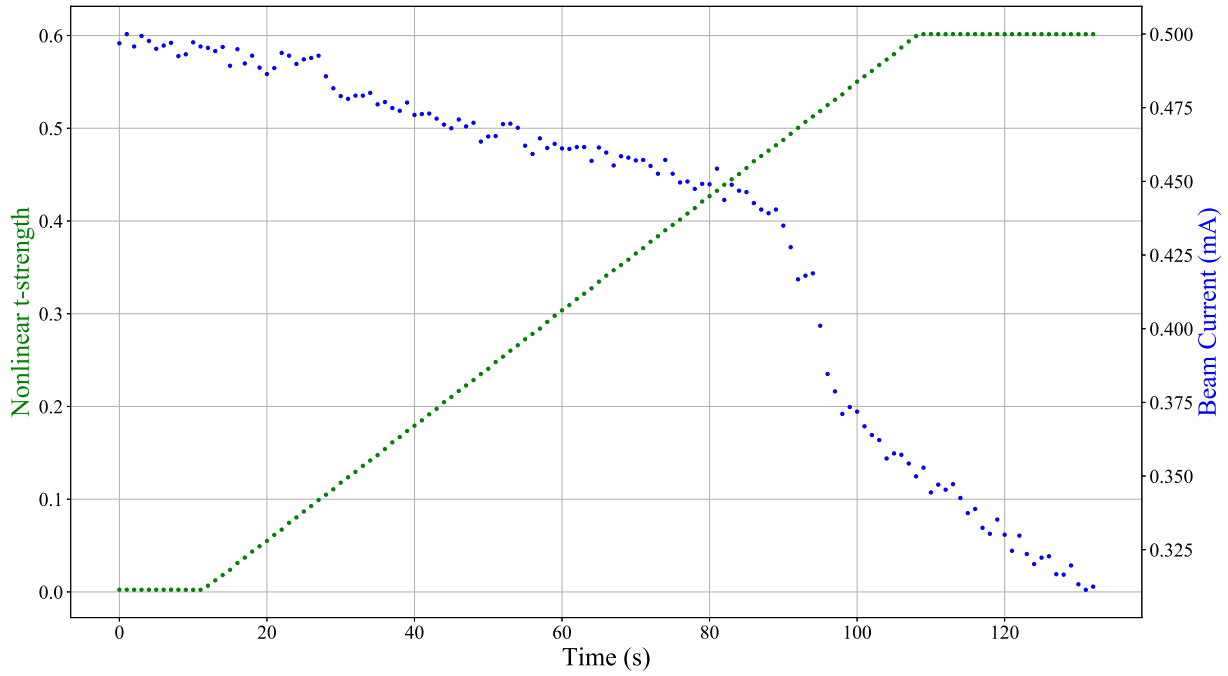

Figure 4.4: Beam Current and Nonlinear t-strength ramping.

The nonlinear magnet was slowly ramped up from $t = 0$ to $t = 0.6$ in 100 seconds, with a starting beam current of 0.5 mA. At $t = 0.146$, the beam is close to a third and fourth order resonance, in which there were no significant losses. At $t = 0.5$, the beam lifetime worsened but improved after moving past the integer resonance. Maintaining a nonlinear magnet strength of $t = 0.6$, the beam is stable, and lifetime improved from the integer resonance.

Figure 4.5 shows the beam current at integer resonance, the nonlinear magnet was ramped up from $t = 0$ to $t = 0.5$ in 15 seconds, with a starting beam current of 3 mA. The beam

was placed on integer resonance for 110 seconds, before abruptly turning off the nonlinear magnet completely.

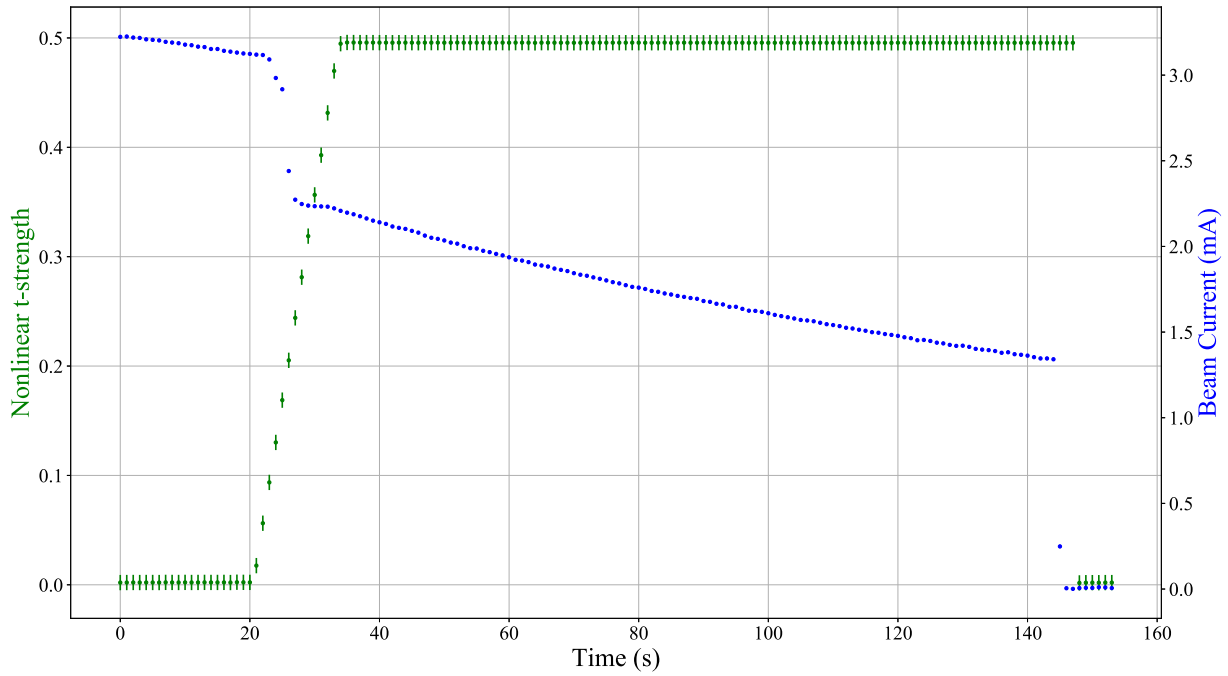

Figure 4.5: Beam Current at integer resonance.

Compared a fast ramp to a slow ramp of the nonlinear magnet, the fast ramp has significant beam loss. However, this was done at a much higher current, and the particle losses can be attributed to intra-beam scattering. Meanwhile, the beam on integer resonance, the beam is stable. With an abrupt turn off the nonlinear magnet, the beam is lost completely. In which without the nonlinear magnet, the beam does not survive the integer resonance.

4.1.1.3 First Experimental Run Amplitude Dependent Tune Measurements

Figure 4.6 shows the tune diagrams for each of the respective t-strength values during the first experimental run. The information shown are the measured tunes (red), model tunes

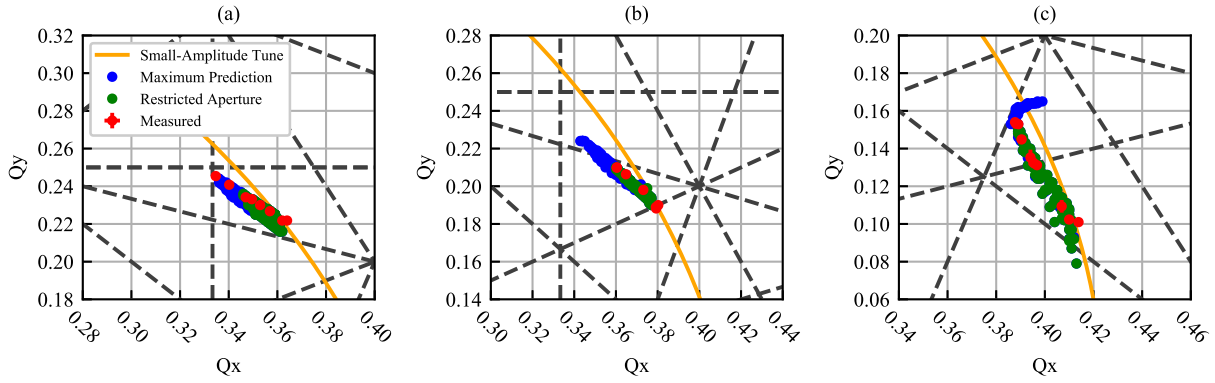

Figure 4.6: Tune diagrams at various t-strength values with model tunes and its mechanical restriction. (a) $t = 0.22$, (b) $t = 0.29$, (c) $t = 0.43$.

with (green) and without (blue) aperture restriction, and the theoretical small amplitude tune (orange).

Table 4.2 is the corresponded measured tune shift for Fig. 4.6.

Table 4.2: Tune Shift Measurements at Different t-strength Values

t-strength	ΔQ_x	ΔQ_y
(a) t = 0.22	0.0334±0.0018	0.0245±0.0018
(b) t = 0.29	0.0198±0.0005	0.0216±0.0010
(c) t = 0.43	0.0261±0.0018	0.0530±0.0018

Table 4.3 lists the maximum vertical kick values and the maximum amplitude in the center of the nonlinear magnet (NL). This is done for each of the respective t-strength values, comparing measurements to the model and its 6 mm aperture restriction (AR) section. Past the model maximum values, the particles are lost due to the aperture of the nonlinear magnet beam pipe. In which by design is the smallest restriction of 5.5 mm vertically in the middle of the nonlinear magnet.

For $t = 0.22$, the maximum measurement matches the model without aperture restriction, unlike other strength parameters. This is due to the beam's fast decoherence of 200 turns. In the AR model, particle loss occurs in 300-500 turns at the restricted section. Conversely,

at higher t-strength for the AR model, particle loss occurs in the order of 10s of turns and agrees with measurements. The model shows that there is much more dynamical aperture to be explored.

Table 4.3: Maximum Values for Amplitude Dependent Tune Shift Measurements at Different t-strength Values

Parameter	**Meas.**	**AR**	**Model**
t = 0.22			
Kick Voltage [kV]	4.80	3.39	4.80
Kick Angle [mrad]	3.43	2.43	3.43
NL Center Amplitude [mm]	4.48	3.18	4.48
t = 0.29			
Kick Voltage [kV]	3.00	4.68	5.18
Kick Angle [mrad]	2.14	2.28	3.71
NL Center Amplitude [mm]	2.98	3.18	5.19
t = 0.43			
Kick Voltage [kV]	2.40	2.40	4.00
Kick Angle [mrad]	1.71	1.71	2.86
NL Center Amplitude [mm]	3.65	3.65	5.19

For the case of $t = 0.43$, Fig. 4.7 shows how the tune shifts with respect to the vertical kick angle. One should note that in the model, varied horizontal kicks were also applied, whereas in the measurements, a single constant horizontal kick was applied. It can be clearly seen that the experiment was limited by the aperture restriction, where the theoretical maximum tune shift at this strength would be $\Delta Q_y = 0.085$.

During the first run, there were limitations during the experiment. For one, orbit bump measurements were made through a straight section in IOTA. This revealed an unexpected restriction of 6 mm in the section. Physical measurements of the beam pipe confirmed that this is indeed the case. This mechanical restriction did not allow for higher amplitude kicks of the beam. A replacement for the beam pipe is currently underway. The electron beam energy was also limited to 100 MeV. Consequently, this leads to large energy spread due to intrabeam scattering (IBS), leading to beam loss while kicking the beam in IOTA. Minimum

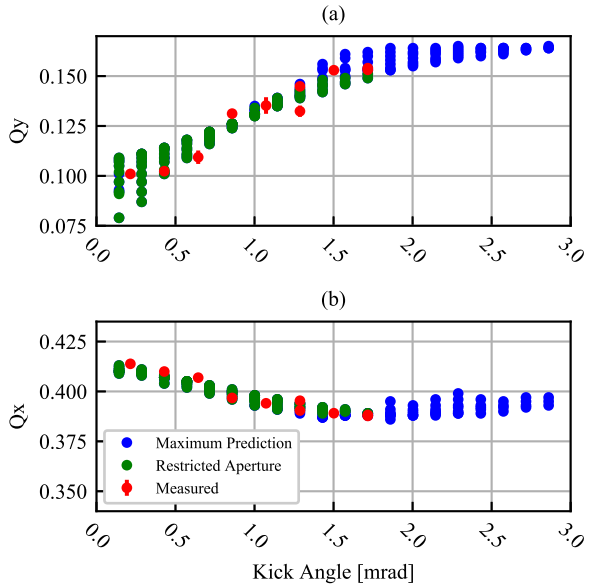

Figure 4.7: Amplitude dependent tune shift, for the case of (a) vertical tune and (b) horizontal tune versus vertical kick at $t = 0.43$.

beam loss occurred at lower beam current (<1 mA). However, at these low currents, there was excess noise in the BPM signal [29].

4.1.1.4 Second Experimental Run Amplitude Dependent Tune Measurements

For the second experimental run, many of the limitations had been fixed and improved. The maximum nonlinear strength measurements with beam position monitors are at a value of $t = 0.49$. The vertical small amplitude tune of $Q_y = 0.042$, where the beam is close to an integer resonance.

The repeated measurement from run one was performed with nonlinear strength of $t = 0.22$. However, in addition, horizontal kicks and diagonal kicks where also performed. Figure 4.8 is the measured amplitude dependent tunes from run 2 (red) and run 1 (green), compared with MAD-X simulations (blue). The tune shift is $\Delta Q_x = 0.0234 \pm 0.002$ and $\Delta Q_y =$

0.312 ± 0.006. The corresponding horizontal and vertical detuning of Fig. 4.8 is shown in Fig. 4.9. The second run measurements is in good agreement with the first run, along with MAD-X simulations. Figure 4.10 is the beam loss after (a) 512 turns, and (b) 8000 turns after the kick. For vertical kicks, the beam occurs less than 2% loss in some cases and, in most cases $\leq 0.5\%$ loss after 8000 turns. For horizontal kicks, the beam occurs $\approx 9\%$ loss at the maximum horizontal kick, this is due to limitation in physical aperture.

To prepare for measurements at nonlinear strength of $t = 0.49$, the beam had to be realigned through the nonlinear magnet. However, at this value, chromaticity was not corrected. Only vertical kicks were performed, and there was up to 50% beam loss after each kick. Figure 4.11 is the measured amplitude dependent tunes (red), compared with MAD-X simulations (blue). The tune shift is $\Delta Q_x = 0.028 \pm 0.002$ and $\Delta Q_y = 0.125 \pm 0.001$. The corresponding horizontal and vertical detuning of Fig. 4.11 is shown in Fig. 4.12. The maximum kick angle is 2.18 mrad. The results are similar to the MAD-X simulation. Figure 4.13 is the beam loss after (a) 512 turns, and (b) 8000 turns after the kick. Below a kick angle of 1.5 mrad, the maximum beam loss is less than 10%.

For future Danilov-Nagaitsev magnet studies, IOTA resonance driving terms would need to be well understood. For operating the beam for nonlinear strength of greater than $t = 0.40$, the chromaticity would need to be corrected methodically in each increasing strength.

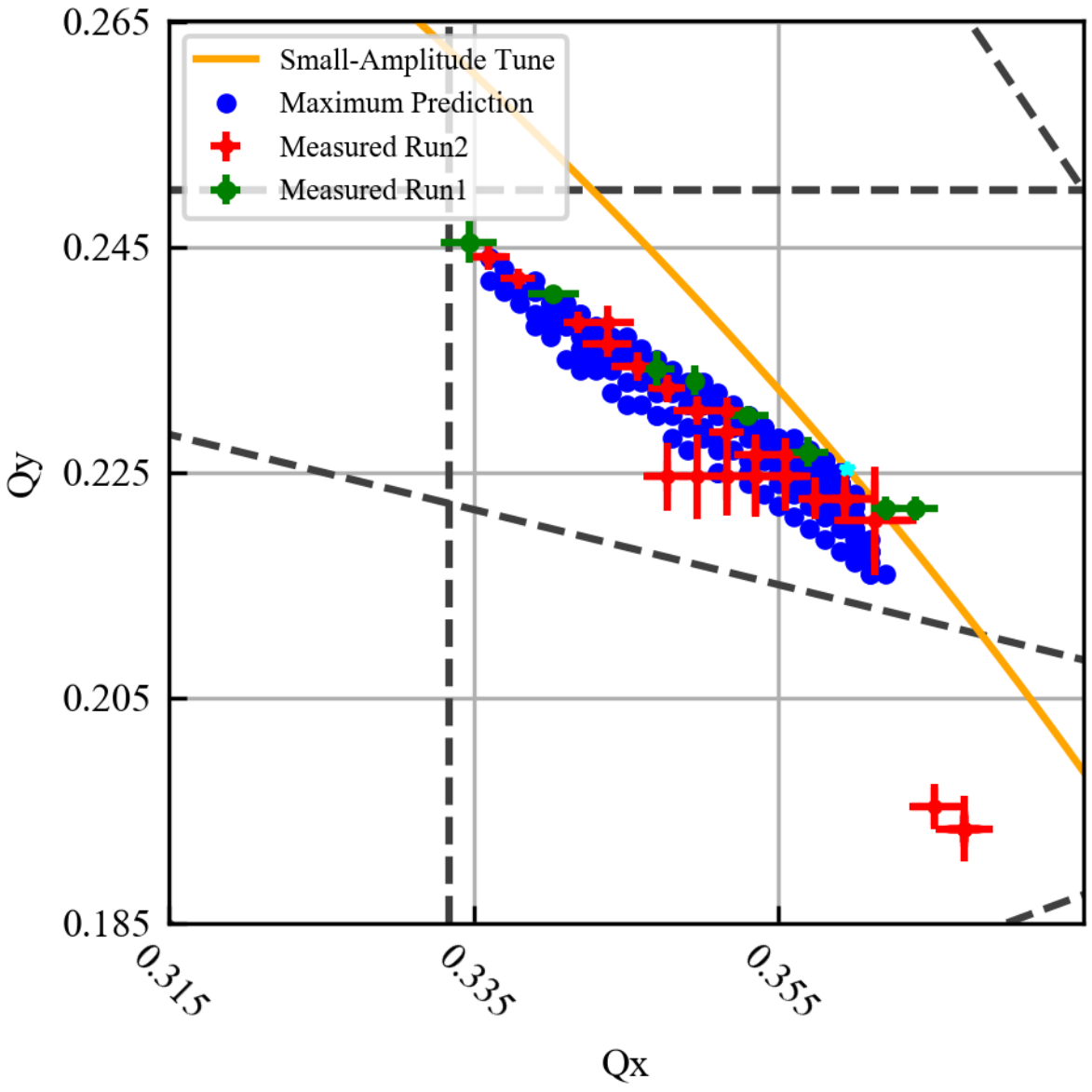

Figure 4.8: Amplitude dependent tune map for the case of $t = 0.22$.

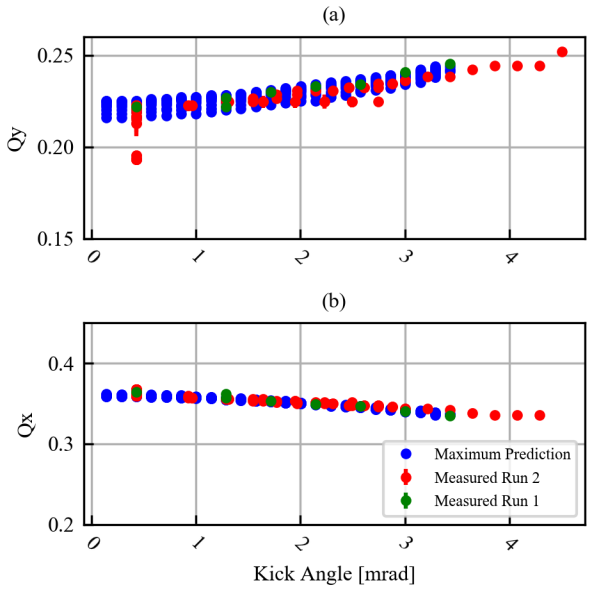

Figure 4.9: Vertical amplitude dependent tune shift, for the case of (a) vertical tune and (b) horizontal tune versus vertical kick at $t = 0.22$.

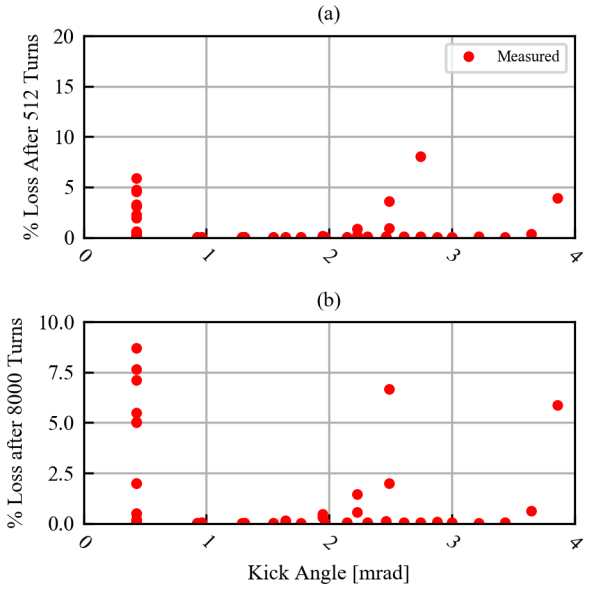

Figure 4.10: Vertical Amplitude dependent beam loss, for the case of (a) % loss after 512 turns and (b) % loss after 8000 turns versus vertical kick at $t = 0.22$.

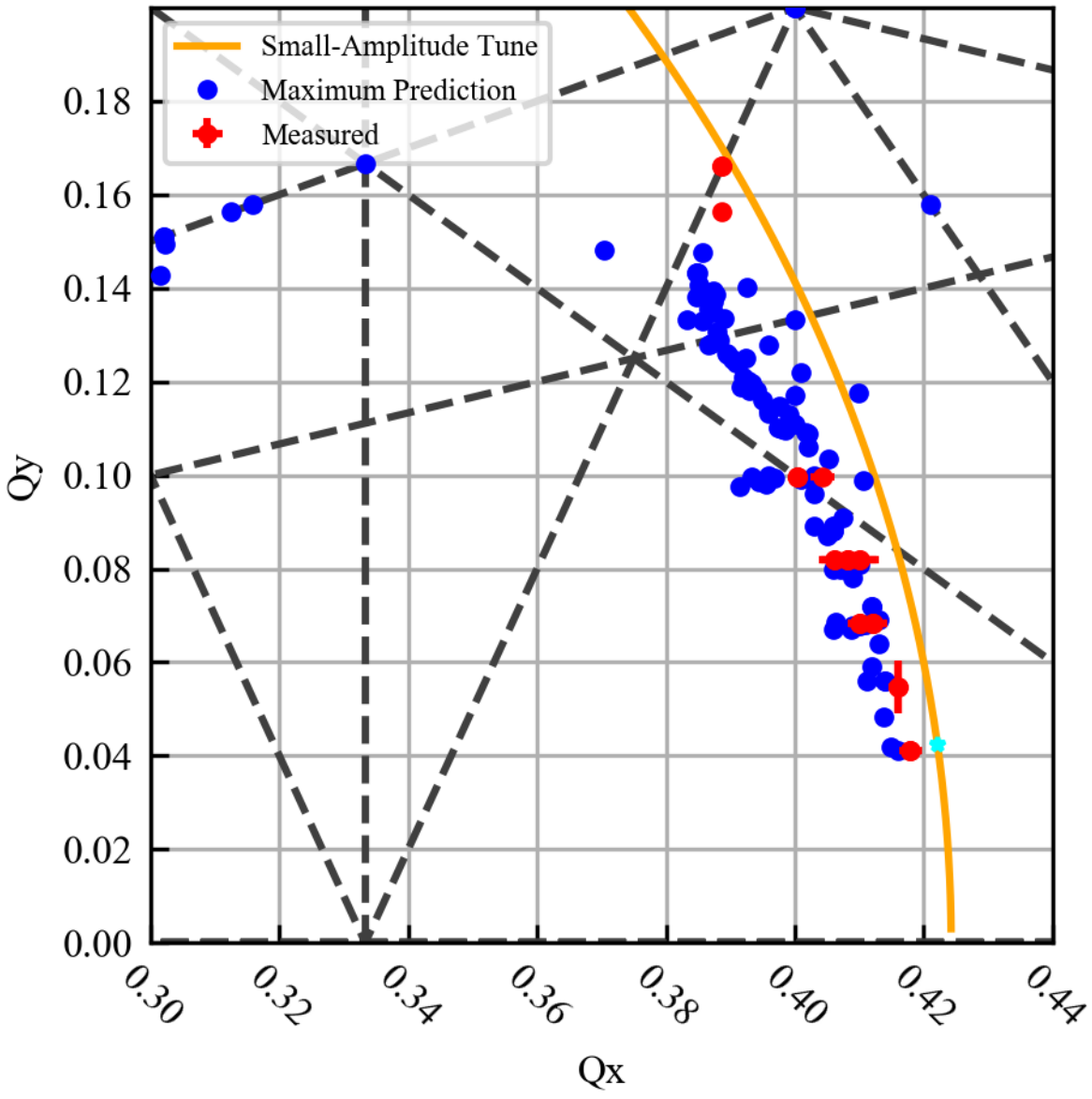

Figure 4.11: Amplitude dependent tune map, for the case of $t = 0.49$.

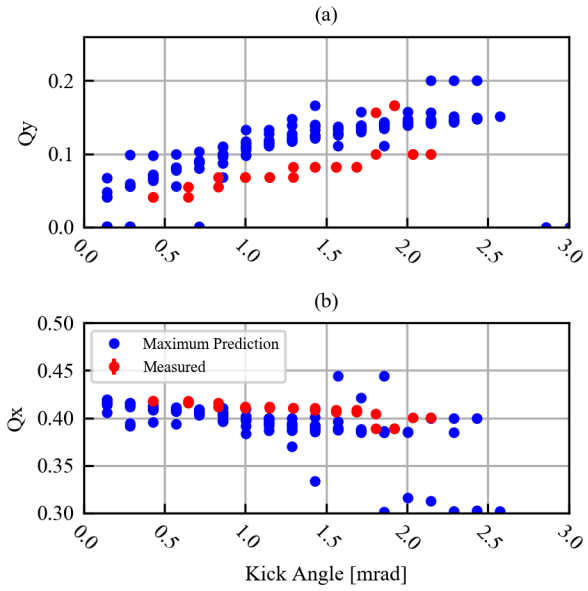

Figure 4.12: Vertical Amplitude dependent tune shift, for the case of (a) vertical tune and (b) horizontal tune versus vertical kick at $t = 0.49$.

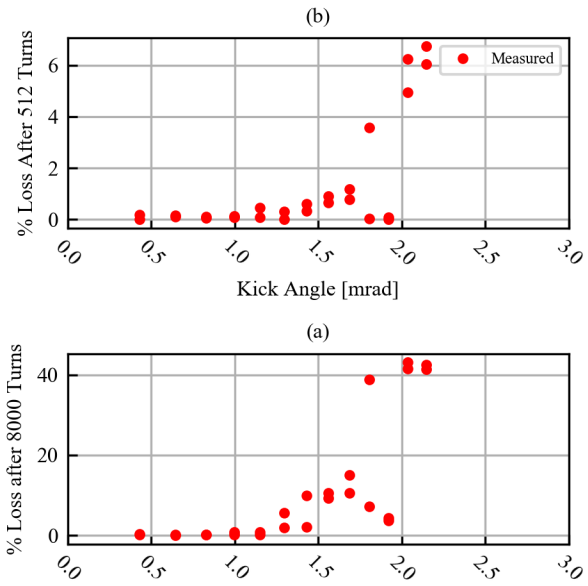

Figure 4.13: Vertical Amplitude dependent beam loss, for the case of (a) % loss after 512 turns and (b) % loss after 8000 turns versus vertical kick at $t = 0.49$.

4.1.1.5 Synchrotron Light Measurements

For large nonlinear t-strength values of greater than 0.5, images of 1 second exposure are recorded from the synchrotron-light diagnostics, systematically increasing the strength. Two beamlets are observed to be stable at the two fixed points in Fig. 4.14, as prescribed by section 2.3.1. Near $t = 0.90$, one of the beamlets slowly decays. This corresponds to the mechanical aperture in the ring. This is of interest as the particle beam survives the crossing of the integer resonance reaching to achieve $t = 0.9$. Demonstration of this nature has not been done in the past, since the discovery in of a Darboux 2-D integrable system in 1901 [30].

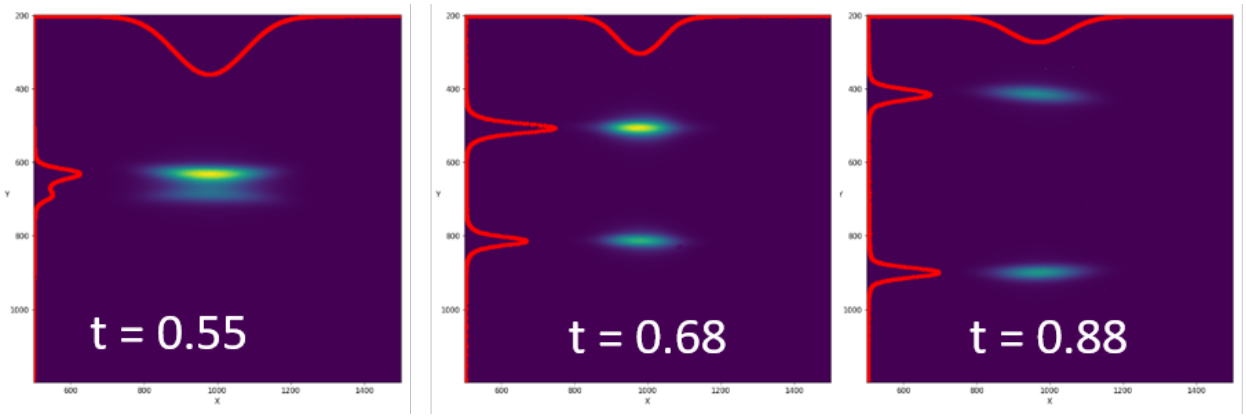

Figure 4.14: Recorded Synchrotron Light Measurements for $t = 0.55$, $t = 0.68$, and $t = 0.88$

Figure 4.15 is the recorded distanced between the maximum intensity of the two beamlets in the M2L synchrotron diagnostics, in blue with the t-strength values are from 0.60 to 0.90 in steps of 0.02. Whereas in orange is the model from section 2.3.1. M2L real measurements were converted to normalized coordinated based of the lattice functions at M2L.

The RMS of the beamlet size was calculated by fitting a Gaussian curve of the horizontal and vertical sum intensity, respectively, from the M2L synchrotron-light diagnostics. From $t = 0.6$ the horizontal RMS beamlet size decreased by 14.25% at $t = 0.86$, while vertically

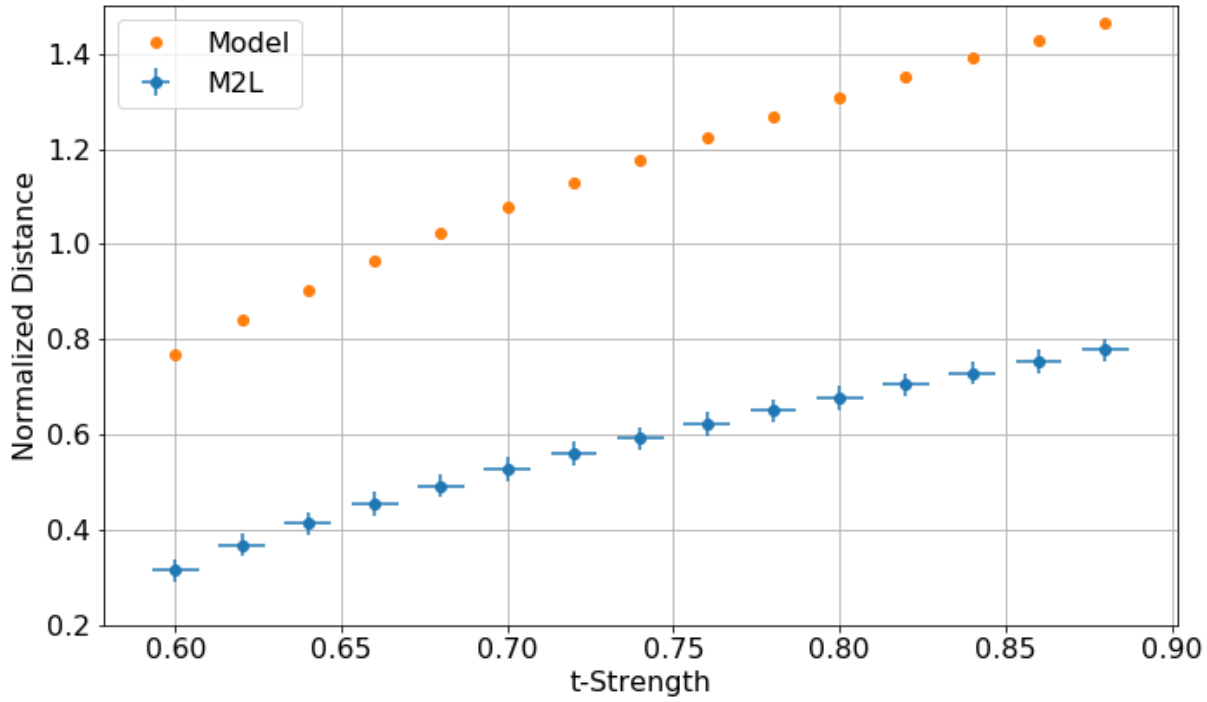

Figure 4.15: Distance between peak intensity of two beamlets.

the beamlet RMS size increased by 12.73%. This is shown in Fig. 4.16(a), where the RMS horizontal measurements are in green, RMS vertical measurements in blue, and t-strength in black. At $t = 0.68$, an instability is observed that is due to lattice imperfection. The beamlets were not lost at this region.

For nonlinear t-strengths of $0.51 \geq t \geq 0.49$, the RMS size was also recorded, as shown in Fig. 4.16(b). The uncertainty in the nonlinear t-strength is ± 0.007. At $t = 0.505$, vertical instability is observed. However, the synchrotron light intensity did not decrease, and the beam is able to survive on integer and near integer resonance.

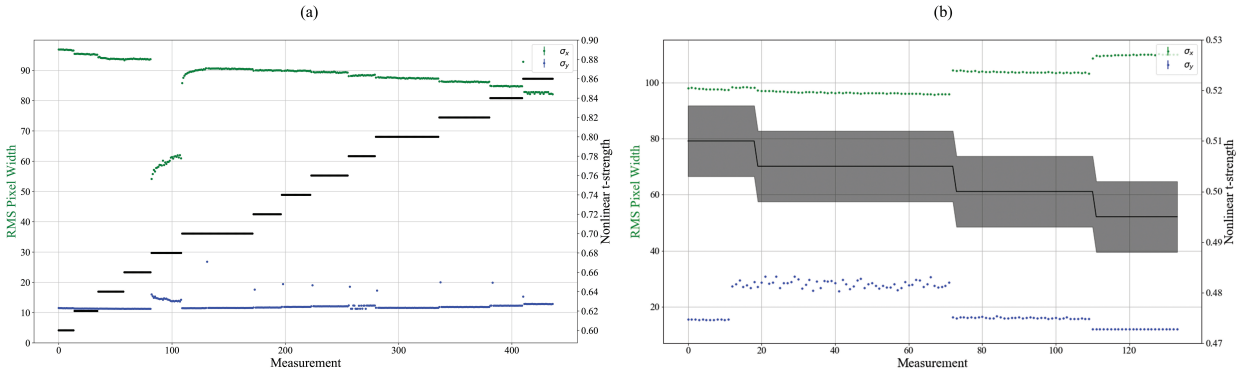

Figure 4.16: Measured beamlet RMS width with corresponding nonlinear t-strength for (a) $0.6 \leq t \leq 0.86$ and (b) $0.0.49 \leq t \leq 0.51$

4.1.2 Summary

The Danilov-Nagaitsev Nonlinear Magnet improves the transverse dynamical aperture of accelerator lattices. The beam successfully survives crossing various resonances, and notably, the integer resonance. In which the beam also survives at the integer resonance. It was also demonstrated that the beam can be split into two beamlets, circulating in the same accelerator. This method can lead into beam extraction in accelerator complexes. The largest observed tune shift during the experimental runs was $\Delta Q_x = 0.0280 \pm 0.0021$ and $\Delta Q_y = 0.125 \pm 0.0016$ at $t = 0.49$. Which would allow for beam stability due to space charge tune shifts. The measured spread of tune frequencies from the nonliner magnet is also in good agreement with MAD-X simulations. The nonlinear magnet paves the way for future accelerator designs for multi-megawatt beam power in high intensity accelerators.

CHAPTER 5

GAS SHEET BEAM PROFILE MONITOR

Minimally invasive diagnostics for low energy proton beam are limited, and innovation is needed to satisfy the needs of diagnosing time dependent collective instabilities and halo formation. Traditional profile monitors such as multiwires and scintillator screens are too destructive to the proton beam, or they measure one-dimensional such as residual gas monitors. In this chapter, the concept and background behind a gas sheet beam profile monitor will be discussed as well as steps in developing one. The basic principle of how it works is by having a gas sheet formed transversely at an angle to the beam direction. Then the proton beam will ionize the gas, leading to ion-electron pair of the gas, and the ions will be collected into a detector system, which will measure the two dimensional transverse profile of the proton beam. The process is depicted in Fig. 5.1. The gas sheet profile monitor can be broken down into three main components, the gas injection, ionization product extraction, and imaging the extraction.

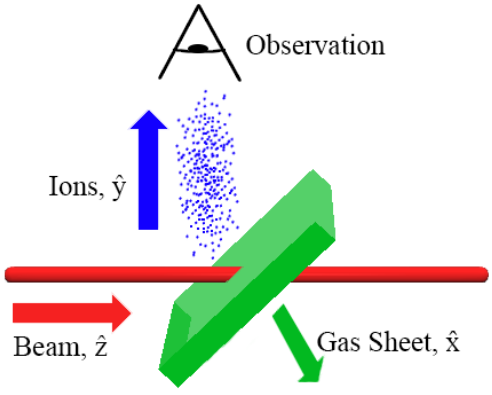

Figure 5.1: Depiction of a Gas Sheet Beam Profile Monitor concept.

5.1 Molecular Kinematics

An atom traveling in a medium can experience different molecular kinematics based on the environment it is in and its own molecular species. An atom's motion before it collides with another moving atom is called the mean free path. This can be expressed as:

$$\lambda = \frac{k_B T}{\pi\sqrt{2} d_0^2 P}, \tag{5.1}$$

where k_B is the Boltzmann constant, T and P are the temperature and total pressure of the environment, respectively, and d_0 is the diameter of the gas molecule traveling in the medium [31]. The mean free path increases when the pressure of the system decreases. Hence, at Ultra-high vacuum, the mean free path is on the order of 1 to 10^5 km. Realistically the atom travels in a closed system, for example, a beam pipe or nozzle. Which can drastically change the kinematics of the ensemble of atoms. It can exhibit viscous flow, molecular flow, or somewhere in between, which is the transition flow. In the molecular flow regime, the gas does not interact with each other, only with vacuum walls. Whereas in the viscous flow regime, the gas can exhibit Laminar or turbulent flow. The regimes are determined by a dimensionless number, the Knudsen number, which is directly proportional to the mean free path of the atoms by the characteristic length.

$$Kn = \frac{\lambda}{D} \tag{5.2}$$

For molecular flow, the Knudsen number is greater than 0.5, while for viscous flow, the Knudsen number is less than 0.01 [32]. The vacuum pressure in most particle accelerator systems is in the range of 10^{-5} to 10^{-11} torr. Thus gas in the system will exhibit molecular flow. For assumptions in the molecular flow regime, gas molecules scatter from a cylindrical

tube exhibit a cosine-like distribution. P. Clausing [33, 34] derived a formula for this pattern as:

$$dN = \frac{d\omega}{4\pi}\xi X n \overline{v} A_s \cos\theta \tag{5.3}$$

where $X = \frac{n_a}{n}$ is the ratio of the number of atoms per unit volume to the total number of particles per unit volume, and A_s is the cross sectional area of the orifice. Assuming Maxwellian particle velocity distribution, $\overline{v}$ can be expressed as:

$$\overline{v} = \sqrt{\frac{8kT}{\pi m}} \tag{5.4}$$

The reduction coefficient is expressed as ξ, and is dependent on the geometries of the orifice. For example, a cylindrical tube of length l and diameter d, at $l \gg d$ give a reduction of:

$$\xi = \frac{4d}{3l} \tag{5.5}$$

At various tube lengths, the distribution pattern will change. Noticeably when the tube length is longer, the distribution will be weighted closer to the center axis. This is usually called a beaming effect from the tube, where the flux of molecules exiting the tube is greater in a small solid angle. Later on the distribution for long cylindrical tubes, Eq. (5.3) was modified by Dayton [35]. Let $p = \frac{l}{d}\tan\theta$, where l is the length of the cylindrical tube and d its diameter. The correction factor ξ becomes

$$\begin{aligned} \xi(p<1) &= 1 - \frac{2}{\pi}(1-\alpha)(\arcsin(p) + p\sqrt{1-p^2}) + \frac{4}{3\pi p}(1-2\alpha)[1-(1-p^2)^{3/2}], \\ \xi(p\geq 1) &= \alpha + \frac{4(1-2\alpha)}{3\pi p}, \end{aligned} \tag{5.6}$$

where the general expression for α for the cylindrical tube with $u = \frac{l}{d} - v$ and $v = \frac{l\sqrt{7}}{3l+d\sqrt{7}}$ is

$$\alpha = \frac{u\sqrt{u^2+1} - v\sqrt{v^2+1} + v^2 - u^2}{\frac{u(2v^2+1)-v}{\sqrt{v^2+1}} - \frac{v(2u^2+1)-u}{\sqrt{u^2+1}}}. \tag{5.7}$$

The general expression for uniform circular cross section tubes agrees with Cole [36] data to within 0.13%. The angle at which the distribution, from circular tubes, falls to half the maximum intensity is proportional to the ratio of the cylindrical diameter to its length. This can be represented as [37]:

$$\theta_{\frac{1}{2}} = 0.84\frac{d}{l} \tag{5.8}$$

The transmission coefficient can be modified to various other geometries of the tubes and orifices, such as rectangular and elliptical. Rectangular orifices will also be considered[38, 39]. For a uniform cross section rectangle orifice the reduction coefficient with $l \gg d$ and $l \gg h$ becomes:

$$\begin{aligned} \xi = \frac{1}{ldh}\Bigg\{ & d^2 h \ln\left(\frac{h}{d} + \sqrt{1+\left(\frac{h}{d}\right)^2}\right) + \\ & dh \ln\left(\frac{d}{h} + \sqrt{1+\left(\frac{d}{h}\right)^2}\right) - \frac{\left(l^2+d^2\right)^2}{3} + \frac{l^3+d^3}{3}\Bigg\} \end{aligned} \tag{5.9}$$

If $l \gg d$ and $l \ll h$, then the reduction coefficient is

$$\xi = \frac{d}{l}\ln\left(\frac{l}{d}\right) \tag{5.10}$$

while lastly for the case of $l \gg d$, $l \gg h$, and $h \gg d$

$$\xi = \frac{d}{2l}\left[1 + 2\ln\left(\frac{2h}{l})\right)\right] \tag{5.11}$$

For the case of any geometric shape thin orifice of length $l \sim 0$, the reduction coefficient becomes:

$$\xi = 1 \tag{5.12}$$

For cylindrical tubes, the beaming effect is demonstrated in Fig. 5.2 with the angular distribution of eq. (5.3) and correction (5.6).

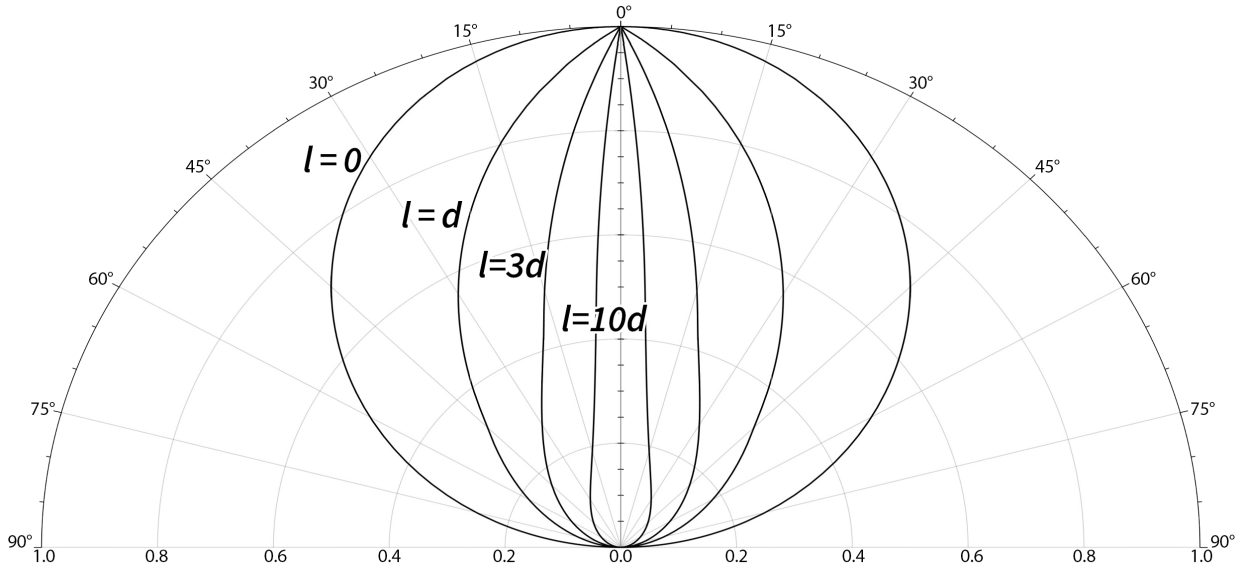

Figure 5.2: Angular distributions of atoms emitted from various length l and diameter d of cylindrical tubes.

Representing Fig. 5.2 in Cartesian Coordinates (Fig. 5.3), the half maximum intensity from eq. 5.8 is readily demonstrated. For example, in Fig. 5.3(a) has a $l/d = 1$, in which the half intensity is at 48.12 deg. Whereas in Fig. 5.3(b) has a $l/d = 10$, in which the half intensity is at 4.81 deg.

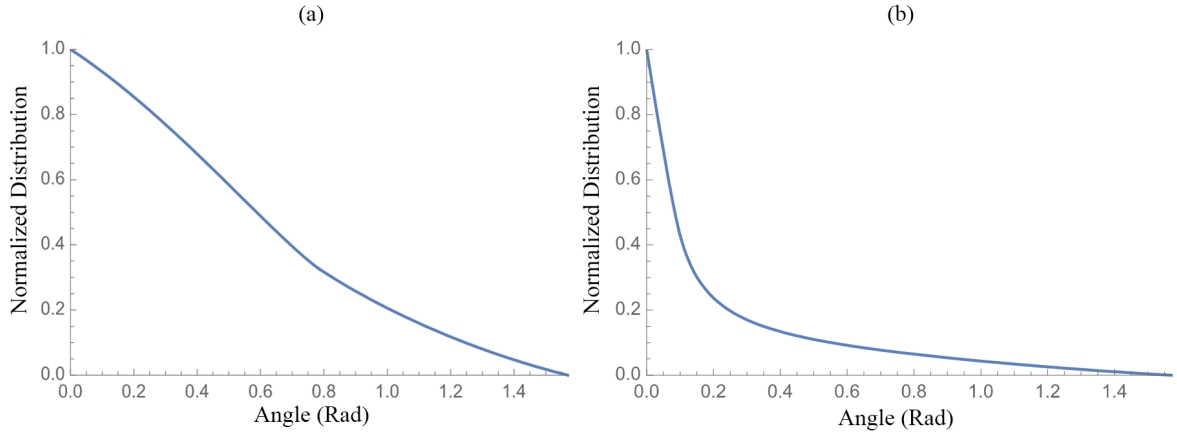

Figure 5.3: Angular distributions with respect to the angle for (a) $l/d = 1$ and (b) $l/d = 10$

Gas mass density can be calculated by rewriting the ideal gas law to:

$$\rho_g = \frac{PM}{RT} \tag{5.13}$$

where P is the pressure, M is the molecular weight, R is the gas constant, and T is the temperature.

5.2 Particles Interaction with Matter

A particle beam traversing through matter, such as a gas sheet, will ionize the gas producing electron-ion pairs. An estimation taking into account excitation, secondary ionization, etc., is derived from measurements of the average energy required to ionize a gas molecule [40–42], thus the number of electron-ion pairs produced per second is:

$$\dot{N} = \frac{dE}{dx}\frac{I_b}{q}\frac{\rho_g, l}{W_i}, \tag{5.14}$$

where dE/dx is the stopping power of protons in the gas, ρ_g is the mass density of the gas, and W_i is the average energy required to ionize a gas molecule. Thus variables that are a dependant of a particle beam are the beam energy and current. While variables for the gas sheet is its thickness and pressure. The implication of the stopping power dE/dx is that the particle beam lose kinetic energy as it transverse through matter.

The particles also exhibit small-angle scattering due to Coulomb interaction from the nuclei of the matter. For this study, it is sufficient to use a Gaussian approximation, encompassing 98% projected angular distribution [43].

$$\theta_0 = \frac{13.6\text{MeV}}{\beta cp} z \sqrt{\frac{x}{X_0}} \left[1 + 0.038 \ln \frac{x z^2}{X_0 \beta^2} \right] \tag{5.15}$$

Where $p, \beta c$, and z are the momentum, velocity, and charge number of the incident particle, and x/X_0 is the thickness of the scattering medium in radiation lengths. The radiation length and stopping power can be calculated or looked up in tables from the National Institute of Standards and Technology (NIST) [44].

5.3 Beam lifetime in IOTA

Due to the nature of the detector, gas is being injected into the accelerator. This will have an effect on the lifetime of the proton beam in IOTA. Thus it is crucial to optimize how much gas is being injected into the accelerator that will not affect the beam lifetime significantly. The lifetime in IOTA is expected to be 38 min, with an average vacuum pressure throughout the ring to be $< 10^{-10}$ torr. To estimate the lifetime in IOTA with the gas sheet profile monitor in operation, the following parameters are used for (eq. 2.31) The beam pipe radius has a radius of 2.5 cm, and without knowing the precise location of the detector, the maximum beta function, of 8 m, is used to determine an estimate of the ring

acceptance $\epsilon_A = 7.81 \times 10^{-5}$ m. The beam parameter in IOTA for protons is $\beta = 0.0728$. Due to strict vacuum requirements in IOTA, it is required to have a vacuum pressure of $< 10^{-9}$ torr in a 1 meter gas interaction region. A gas sheet thickness of 0.3 mm of the gas density of $2.31 \times 10^{-13} \frac{g}{cm^3}$ in a 1 meter section will have a pressure of 1.32×10^{-9} torr. The lifetime in IOTA with a gas sheet profile monitor in operation is then approximately 20 minutes. This decreased in a lifetime is acceptable and allows for other experiments to run in parallel with the diagnostic device. For other gas pressures, the beam lifetime is plotted in Fig. 5.4

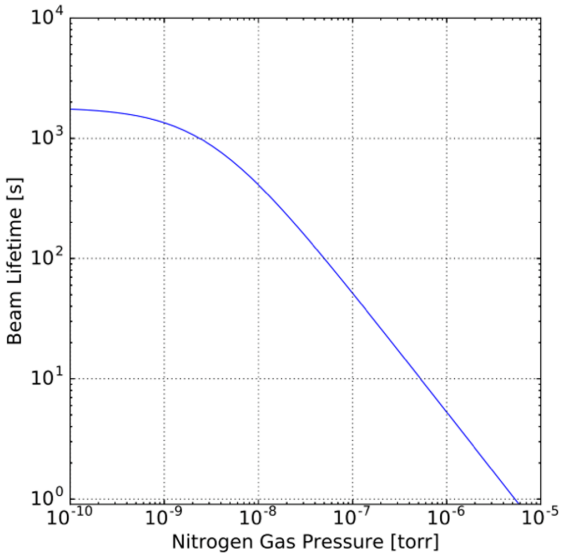

Figure 5.4: Beam Lifetime with respect to nitrogen gas pressure

5.4 Simulation of Rectangular Capillary

To understand the gas sheet injection system, the distribution at various nozzle-skimmer offsets and varying distances, simulations were performed [45]. The gas sheet system was modeled based on the detector to be used in the rapid cycling synchrotron at J-PARC

[46]. The simulation software used is Molflow+ [47], which is developed at CERN. The dimensions of the system that was modeled and simulation were: a gas reservoir volume 7.5 cm^3, a rectangular nozzle 50 x 0.1 x 100 mm (width x height x length), and a rectangular skimmer of dimensions 60 x 0.3 x 0.5 mm. The model in Molflow+ is shown in Fig. 5.5.

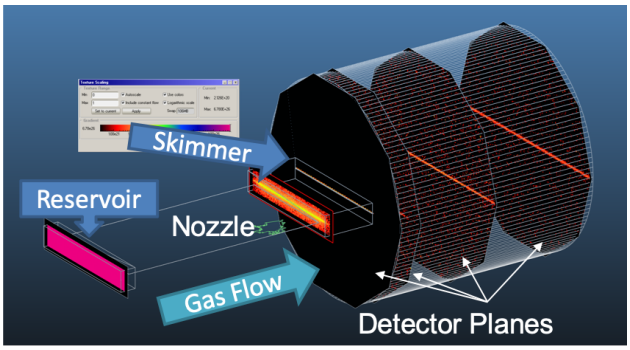

Figure 5.5: Molflow+ model.

The simulation was set up such that the particles were pumped out downstream of the model and considered removed. The nozzle to skimmer distance for the simulation was varied 5, 15, and 25 mm. Additionally, simulation with offset axis of the nozzle skimmer configuration was performed. The distance between the nozzle and skimmer was fixed at 25mm, and the skimmer was offset on its minor axis by 0.1, 0.5, and 1.0 mm. To determine the gas distribution and spread, detector planes were placed at 0.1, 10, 50, and 100 mm after the skimmer, along the gas flow direction. The grid size for each detector plane used 100 cells per centimeter.

Figure 5.6 shows the gas distribution along the minor axis at various nozzle to skimmer distances. Figures 5.6(a), 5.6(b), 5.6(c), and 5.6(d) correspond to detector planes at 0.1. 10, 50, and 100 mm, respectively. As the distance between the nozzle and skimmer decreases, the distribution outside the core the gas sheet becomes more prominent, as the gas sheet flows to the end detector plane. However, the trade off is that the density in the core of the gas sheet increases at all planes.

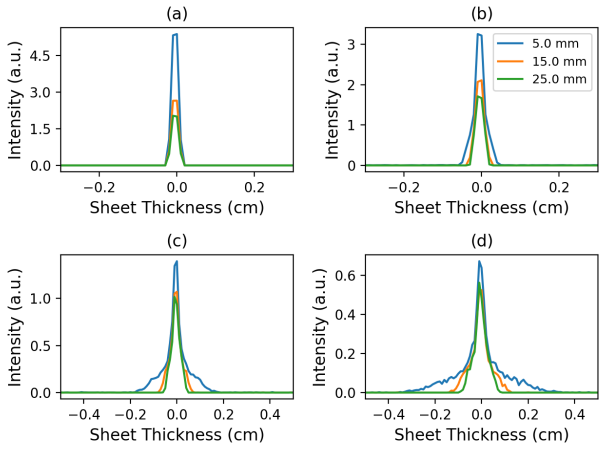

Figure 5.6: Gas distribution with varying nozzle-skimmer distances.

Table 5.4 lists the full-width half max (FWHM) of the distribution for each detector plane for varying distances. For each nozzle-to-skimmer distance, the FWHM grew by ∼0.2 mm over a span of 100 mm.

Table 5.1: FWHM with a various nozzle to skimmer distances from Fig. 5.6.

Distance	**0.1 mm**	**10 mm**	**50 mm**	**100 mm**	**Units**
5.0	0.22	0.25	0.31	0.42	mm
15.0	0.22	0.27	0.33	0.44	mm
25.0	0.22	0.28	0.33	0.41	mm

Figure 5.7 shows the gas distribution along the minor axis at various skimmer offsets, with the same detector plane locations, as mentioned previously. Somewhere between an offset of 0.1 mm and 0.5 mm the intensity of the sheet drops by order of magnitude. This can be seen in Fig. 5.6 and Fig. 5.7, the intensity of the core decreases with increasing distance from the skimmer.

Table 5.4 lists the FWHM values for the various nozzle-skimmer offsets at each of the four detector planes. At 50 mm downstream, there is a noticeable increase in the FWHM for an offset of 0.5 and 1.0 mm. With no offset and the nozzle-skimmer distance at 25

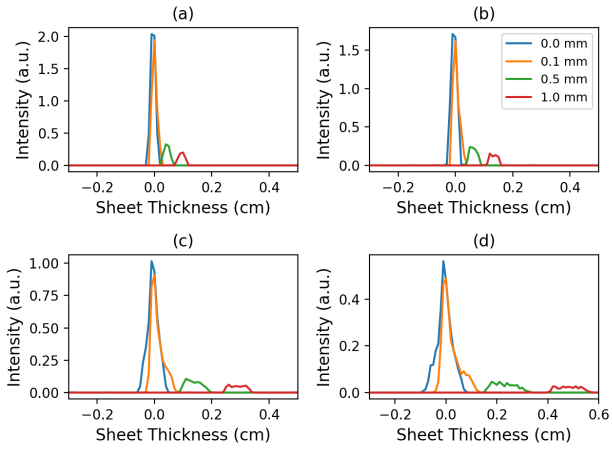

Figure 5.7: Gas distribution with varying skimmer offset.

Table 5.2: FWHM of nozzle-skimmer offsets.

Offset	**D1**	**D2**	**D3**	**D4**	**Units**
0.0	0.22	0.28	0.33	0.41	mm
0.1	0.19	0.21	0.28	0.36	mm
0.5	0.27	0.37	0.73	1.19	mm
1.0	0.29	0.38	0.82	1.32	mm

mm, the FWHM of the sheet measured 100 mm downstream is 0.41 mm. Using the small angle approximation, the divergence of the sheet is ≈0.002 radians. If it is assumed that the rectangular capillary is a super position of cylindrical capillary, then the half intensity angle can be calculated using Eq.(5.8). Thus, the half intensity angle is expected to be ≈0.84 mrad, and the expected FWHM at detector plane four is 0.22 mm. The discrepancy between the two is likely due to the assumption that a rectangular capillary is a superposition of cylindrical tubes is not entirely valid.

5.5 Gas Sheet Test Stand

A test stand is constructed to characterize the gas sheet density and shape for the gas injection system of the gas sheet beam profile monitor. The test stand was built and is in the NML building at Fermilab. A cold cathode pressure gauge attached to a cylindrical vacuum tube with a 1 mm hole is used to measure the gas density and profile. The tube is moved inside a vacuum environment measuring the pressure at various three dimensional points, where the final gas sheet is of concern. The test stand is configurable, where various nozzles and skimmers and be interchanged. The distance between the nozzle and skimmer can also be changed. The gas sheet test stand can be seen in Fig. 5.8 with the labeling of key components.

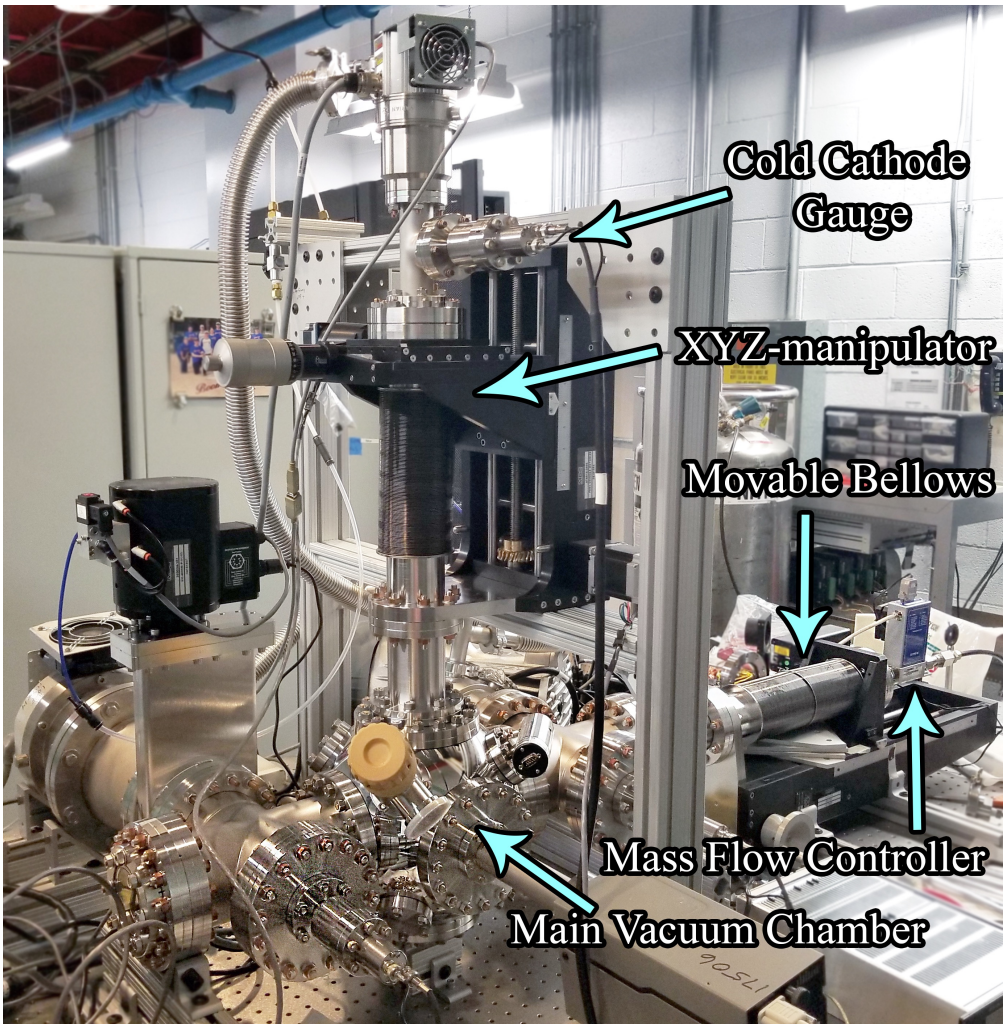

Figure 5.8: Gas Sheet Test Stand.

The gas sheet test stand is constructed with various vacuum hardware that was cleaned to meet ultra high vacuum requirements. A compressed gas bottle of nitrogen is connected to a mass flow controller that can vary the gas flow from 77 to 10,000 sccm. The mass flow controller allows for the gas to be injected into a cylindrical reservoir of 927 cm^3. At the other end of the cylindrical reservoir, a nozzle can be attached. The reservoir is also connected to a movable bellow. The movable bellows which can be used to change the distance between the nozzle and the skimmer. The gas is then expanded into the first vacuum chamber before it reaches a skimmer. The first vacuum chamber has a volume of 4884 cm^3 and has a turbomolecular pump (TMP) with a pumping speed of 145 l/s attached to it. A skimmer is fixed in a holder between the first vacuum chamber and the main vacuum chamber. The main vacuum chamber is where the movable detector device is. The main vacuum chamber has a volume of 9430 cm^3, with a TMP attached to pumping speed 250 l/s. This setup is depicted in Fig. 5.8, and its cross-sectional drawing in Fig. 5.9.

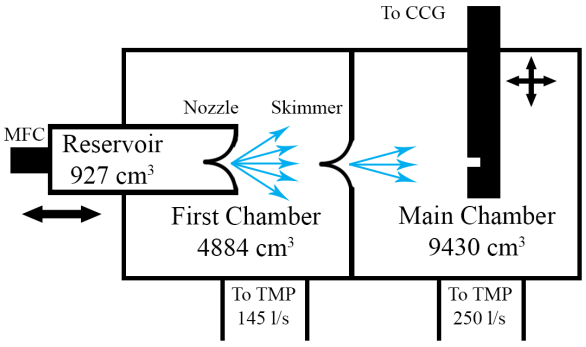

Figure 5.9: Cross-section sketch of gas sheet profile apparatus setup. Blue arrows depict the expansion of gas flow.

Figure 5.10 is the cross-section CAD drawing of the gas sheet test stand showing the holder for the rectangular nozzle and skimmer. The same mechanical design will be used for injecting gas into a beamline and setup at Crocker Nuclear Laboratory test.

The molecular species used for the gas sheet is nitrogen. Nitrogen has a molecular weight of 28 g/mol. The average energy required to ionize nitrogen for an electron beam and proton

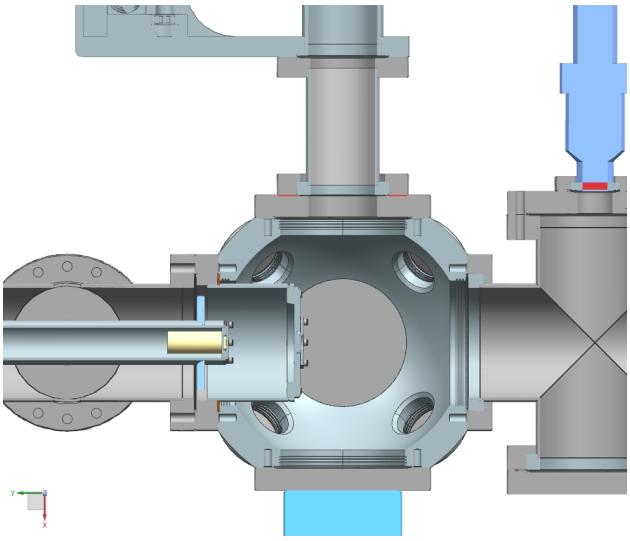

Figure 5.10: CAD cross-section of the gas sheet test stand.

beam is 34 eV and 36 eV, respectively. The current target design for the gas sheet monitor is built and optimize around IOTA, where the sheet has no more than 1% effect on the lifetime of the beam. If we were to assume the gas sheet thickness of 0.2 cm, the pressure of the sheet would have to be 1.2×10^{-7} torr [48]. At room temperature, this equates to a gas density of 1.8×10^{-13} g/ccm by using Eq. 5.13.

5.5.1 Method

When the test stand is under ultra high vacuum, the gas can be injected into the system. The standard operating procedure for measuring the gas distribution of a skimmer-nozzle configuration in the test stand is as follows:

1. Establish background pressure

2. Move the detector to the first position of the scan

3. Inject 150 sccm of nitrogen gas until cold cathode gauge read back plateaus

4. Turn off injection, and wait until background pressure is reestablished
5. Move to next vertical position
6. Repeat steps 3-5 until a full vertical scan is complete
7. Move to next horizontal position and repeat steps 3-6 until a full horizontal scan is complete
8. Move to the next longitudinal position and repeat steps 3-7 until a full longitudinal scan is complete

The typical time it takes to do a full transverse scan in steps of 2 mm for a 20 mm by 20 mm grid is approximately 3.5 hours, by automation using ACNET.

5.5.2 Conical Nozzle Scans

The first operational test in utilizing the gas sheet profile monitor was to test the gas distribution produced by a single conical nozzle. This was performed as a baseline measurement and to understand our test stand operations. Then the second test was to use two identical conical nozzles. This run of tests would measure the gas distribution based dependent on the nozzle-skimmer distance. Figure 5.11 is a picture of one of the conical nozzles. Both of the conical nozzle's dimensions has a length of 6.99 mm, base diameter of 12.70 mm, and orifice diameter of 0.20 mm.

The full-width-half-maximum (FWHM) is determined by using the maximum peak centerline, with a function that uses a spline interpolation. The systematic uncertainty of the gas distribution position transversely, which includes the size of the detector hole and stepper motor resolution, is ± 0.711 mm. The uncertainty of the distance between the nozzle and the skimmer is ± 0.114 mm.

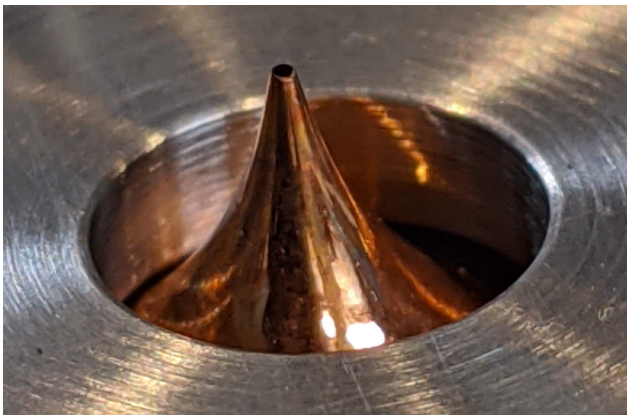

Figure 5.11: Conical Nozzle

Figure 5.12 shows the gas distribution produced by a single nozzle, using a 1 mm step size scan. The FWHM of this figure is 14.56 mm at a location 4.52 mm away from the nozzle.

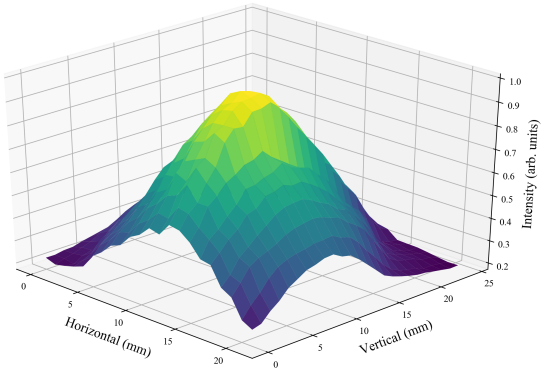

Figure 5.12: 2D scan of a single nozzle located 4.52 mm away.

Figure 5.13 is a transverse profile scan at three different detector planes of 4.52, 9.60, and 14.68 mm away from the skimmer, with a transverse step size of 2 mm. The skimmer-nozzle (S-N) distance is 31.35 mm. The intensity is normalized to the maximum peak located, which is located at the plane of Fig. 5.13(c) (4.52 mm). This peak intensity is four times greater than the peak at plane Fig. 5.13(a) (14.68 mm).

The center-line intensity can be compared at different skimmer-nozzle distances, as shown in Fig. 5.14 with the detector located 4.52 mm from the skimmer. The highest intensity

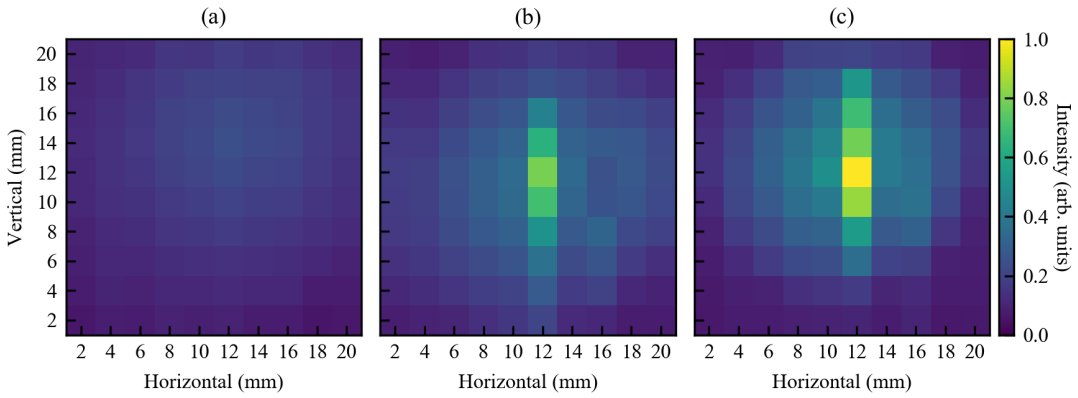

Figure 5.13: Slices of the transverse plane at distances of 14.68 mm (a), 9.60 mm (b) and 4.52 mm (c) from the skimmer. The skimmer-nozzle distance was 31.75 mm.

is when the S-N distance is at 31.75 mm, were it is two times higher than the intensity of distance 47.62 mm. There is also a much more significant peak at S-N = 31.75 mm, indicating the skimmer is closer to sampling the correct subset of gas molecules coming from the nozzle than the other two S-N distances measured. The current smallest FWHM achieved was 8.88 mm vertically, and 3.32 mm horizontally, at a skimmer-nozzle distance of 31.75 mm, measured 4.52 mm from the skimmer. Table 5.3 is the FWHM at various skimmer-nozzle distances and detector locations [49].

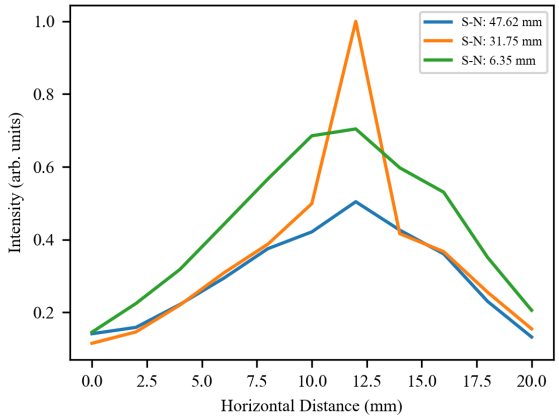

Figure 5.14: Horizontal profile at different skimmer-nozzle distances, measured 4.52 mm from the skimmer.

Table 5.3: Horizontal and vertical FWHM at various S-N distance and detector locations.

Detector Location	**FWHM (mm)**	
S-N Distance = 6.35 mm	**Vert.**	**Horiz.**
z = 4.52 mm	15.69	11.65
z = 9.60 mm	20.78	12.83
z = 14.68 mm	23.18	19.24
S-N Distance = 31.75 mm		
z = 4.52 mm	8.88	3.32
z = 9.60 mm	9.72	4.27
z = 14.68 mm	23.9	18.77
S-N Distance = 47.62 mm		
z = 4.52 mm	11.65	12.40
z = 9.60 mm	14.93	15.51
z = 14.68 mm	24.51	18.42

The Gas Sheet Test Stand performs as expected using conical nozzles as a baseline measurements.

5.5.3 Rectangular Nozzle and Slit

The rectangular nozzle dimension is (12.75 x 0.60 x 50.00) mm, while the skimmer dimension is (12.75 x 0.60 x 0.89) mm. The distance between the nozzle, and skimmer is 4.76 mm and the detector location 5.52 mm away from the skimmer. The XYZ manipulator was set at a fixed horizontal position, and the detector swept vertically for 50 mm at a constant speed of 0.135 mm/s. Where the cold cathode gauge can record the pressure at the given location. Then the next horizontal position is positioned and the sweep begins again until it reaches 8 mm. The volumetric flow rate of the nitrogen gas was 300 SCCM. Figure 5.15 is the rectangular configuration scan. The RMS width of the distribution is 12.825 mm, which corresponds to a thickness of 6.65 mm at a 42° sheet angle. The RMS varies ±0.54 mm horizontally. The large RMS width can be attributed to the residual background nitrogen gas in the first chamber into the main chamber, and the initial volumetric flow rate would need to be reduced or have additional pumping speed in the first chamber.

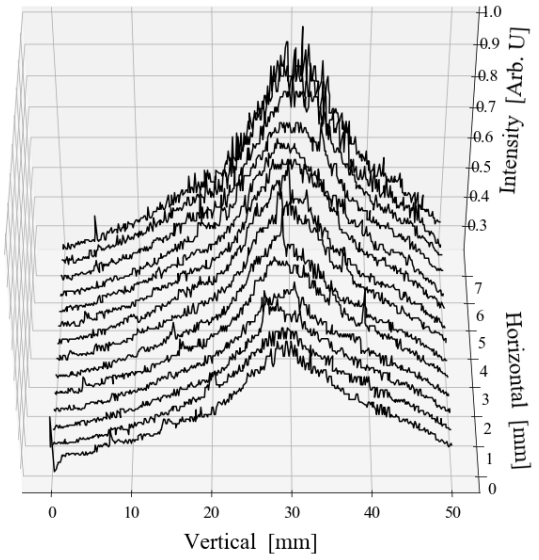

Figure 5.15: Rectangular Nozzle and Skimmer Intensity Scan.

To reduce the residual background nitrogen gas from the first chamber the mass flow controller was configured such that the volumetric flow rate of nitrogen gas is 38 SCCM. This was done by pulsing the injection with the minimum flow rate every other second. A constant pulsation of gas effects the background pressure no more than 10% in fluctuation in the first and main chamber. Measurements with a grid scan method is then used to determine the profile of the rectangular nozzle and skimmer configuration. The XYZ manipulator was moved vertically in steps of 0.1 mm and 0.5 mm horizontally. A moving average of is set on vertical measurement scans. Figure 5.16 is a scan with skimmer nozzle distance of 12.7 mm. The RMS width of the distribution is 0.610 ± 0.302 mm.

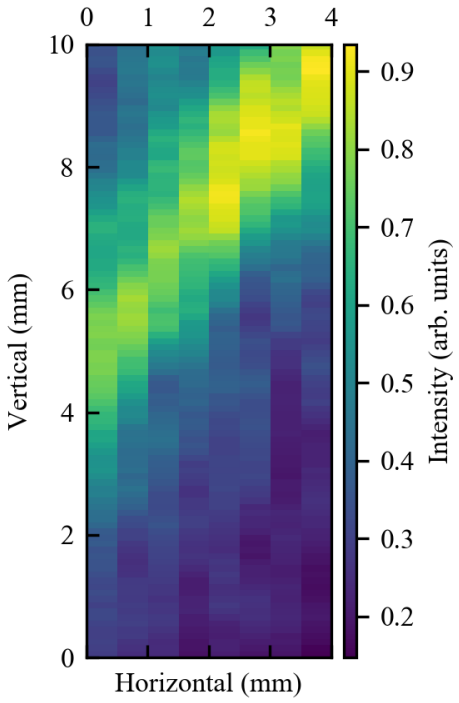

Figure 5.16: Rectangular nozzle and skimmer intensity scan with pulsed gas.

5.6 Electrode Stack

The by-product, electron-ion pair, from beam ionization of the gas sheet is extracted. To do this, the created ions accelerate through a uniform electric field from the electrode stack to a Microchannel Plate (MCP). The electric field is created by biasing the individual copper plate. The simulated field was done using Poisson Superfish, a 2D field solver [50]. Figure 5.17 is the potential contours of the electrode stack assembly, that has azimuthal symmetry. The interaction region where the beam will ionize the gas sheet is located at the vertical distance of 10 cm in Fig. 5.17. The ions will traverse with the increased vertical distance towards the MCP located at 25 cm. While in Fig. 5.18 demonstrates the vertical E_z, and radial E_r electric field component along the center, the voltage applied to the conductors, are simulated to have a 2% error. The average vertical electric field in which the ions will travel along is $E_z = 130$ V/cm, with zero radial electric field component.

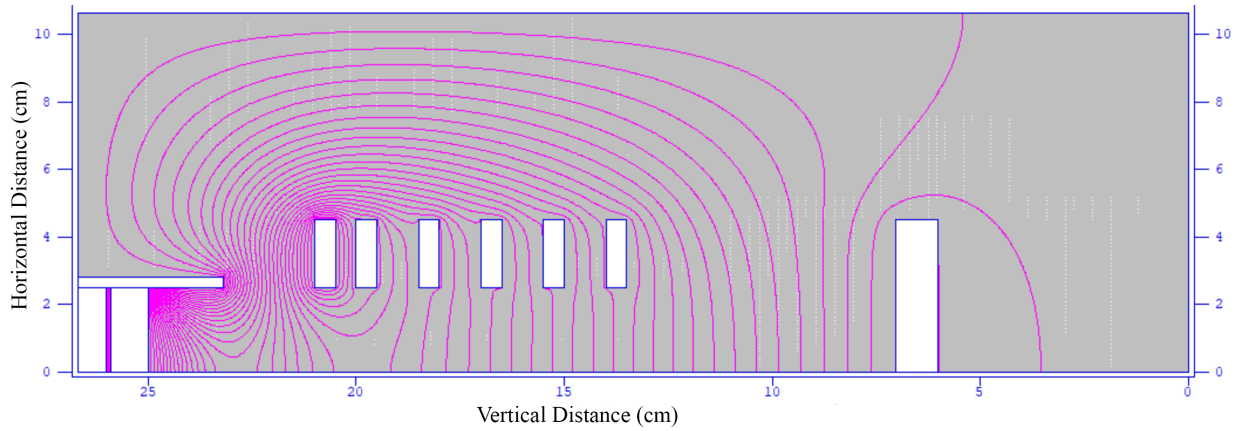

Figure 5.17: Electrode stack simulation, where pink lines are potential contour lines. Vertical distance above 22 cm is the MCP system, and the blue bordered boxes are the conductors.

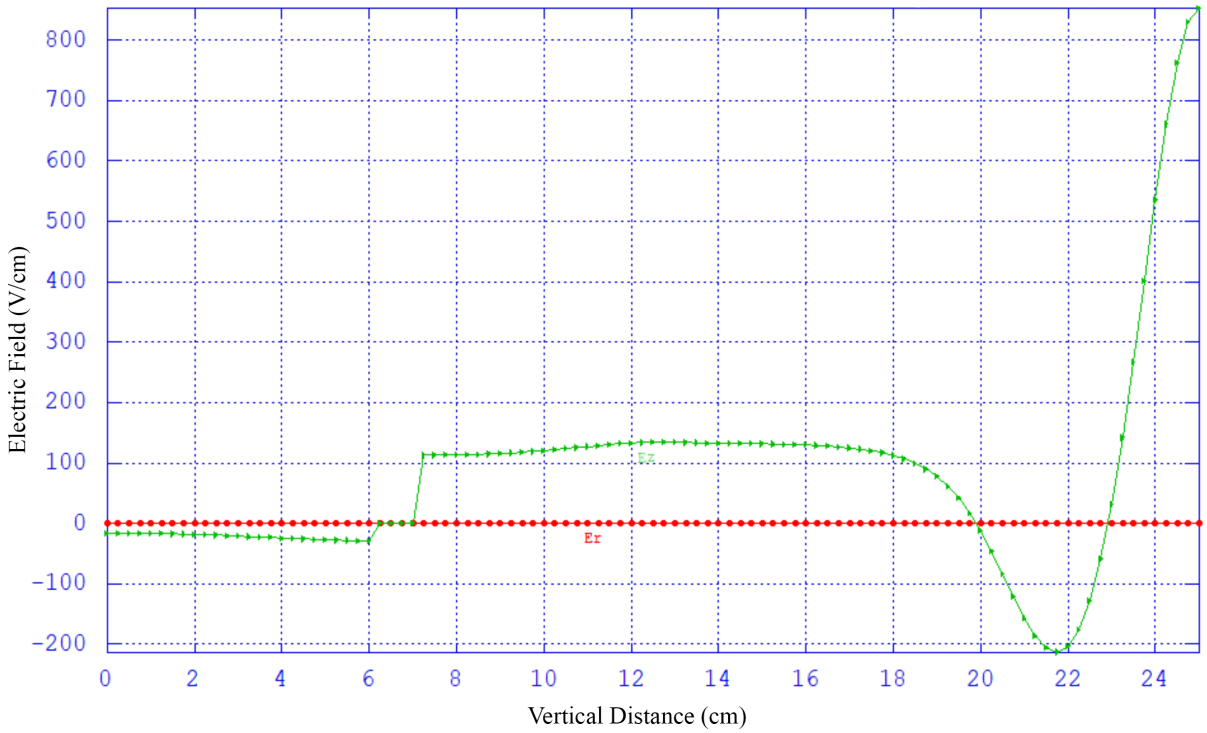

Figure 5.18: Radial E_r and vertical E_z electric field through the center of the electrode stack.

The mechanical consideration of building the stack is to make sure the annulus plates are supported by a non-conductive material. The threaded rod and spacers between the disks are made out of PTFE material, with a tolerance of ±0.01". Figure 5.19 is the completed drawing of the electrode stack with wiring to the feedthrough. The top portion in the figure is a place holder with the proper dimension of the MCP.

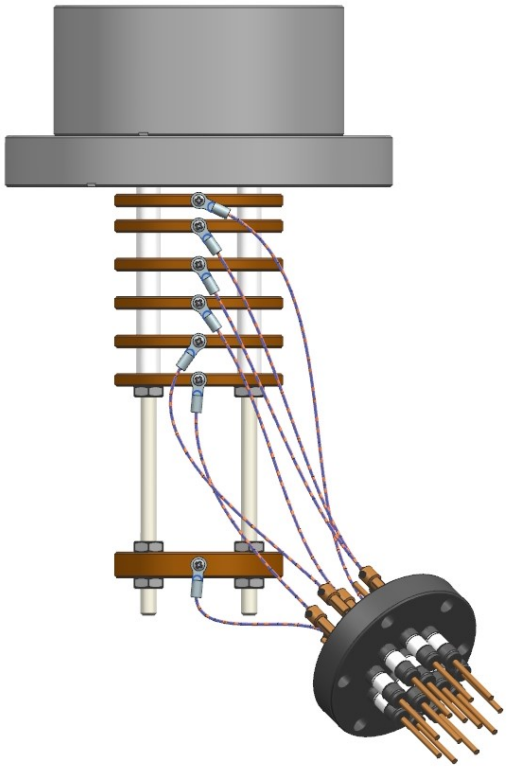

Figure 5.19: Electrode Stack Assembly

5.7 Imaging

The ions produced travel along the electric field from the Electrode Stack to a Microchannel Plate (MCP). The MCP is an off-the-shelf product with a 40mm active area, with a 10 micron channel diameter and a gain of 10^4. The amplified signal is then illuminated by a P-43 phosphor screen. The illumination is imaged by a CCD camera, where the data can be processed in determining the transverse profile.

For consideration of a semi turn-by-turn operation in IOTA for diagnosing beam halo evolution, it is recommended to upgrade the imaging system. The MCP would need to have a duel chevron configuration with a smaller channel diameter as well as a different scintillator with a faster decay time that is comparable to the specification, frames per second, on the camera, and the revolution period of 1.83 μs, for protons in IOTA.

5.7.1 Resolution

The resolution for a beam measurement based on using the gas sheet profile monitor has numerous contributing factors. These are the microchannel plate resolution, camera resolution, gas sheet thickness, ionization spread, nonlinear external fields, and beam induced distortion via space-charge. The first two are hardware related specification. The gas sheet thickness contributes to the vertical resolution. With a gas sheet thickness d, a particle, traveling $+z$ direction, can ionize the gas sheet anywhere in the segment $\{(x, y, \frac{y}{\tan\alpha}); (x, y, \frac{y}{\tan\alpha} + \frac{d}{\sin\alpha}\}$, where α is the tilted angle of the gas sheet with respect to the beam [51]. Thus the imaging broadening from the thickness of the gas sheet is $\sigma = d/\sin\alpha$. This is shown in Fig. 5.20.

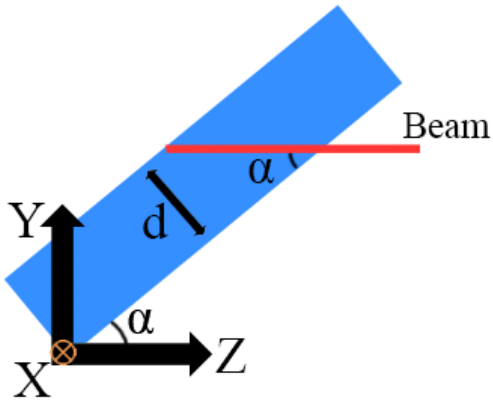

Figure 5.20: Schematic of the particle beam (red) interacting with the gas sheet (blue).

5.8 Setup at Crocker Nuclear Laboratory

The prototype gas sheet beam profile monitor (GSBPM) will be tested at Crocker Nuclear Laboratory (CNL), tentatively at the end of 2020. In order to ensure the vacuum quality of less than 10^{-8} torr in the gas sheet beam profile monitor, the system will be isolated from Crocker Nuclear Laboratory beamline. The beam profile monitor will have a titanium window of thickness 0.127 mm. Where as the Crocker Nuclear Laboratory end of their beam-line will have a standard Kapton window of thickness 0.3 mm. The profile monitor is on a movable cart and the facility beamline can be extended to minimize the gap of air between the two windows. The setup is depicted as a CAD drawing in Fig. 5.21. While using Eq.(5.14) and Eq.(5.15) is useful for a single material, numerical simulation is needed when dealing with multiple materials. Using G4Beamline, a particle tracking simulation program with the interaction of matter, the beam distribution and energy can be determined. In subsection 5.8.1, the analysis is performed with the given windows, and varying air gap.

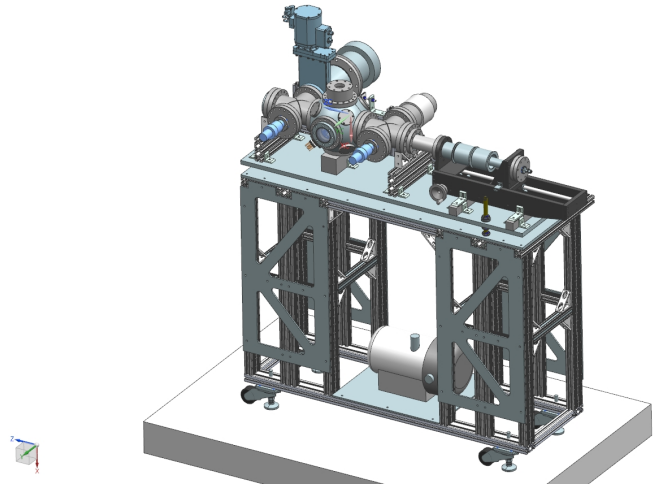

Figure 5.21: GSBPM setup at Crocker Nuclear Laboratory

5.8.1 Simulation of Particle Interaction with Matter

The materials for isolating the vacuum system from the atmosphere are already in hand, and the only material properties than can be altered is the gap of air between the two windows. Hence, the two main parameters that affect the final beam energy and distribution are the initial beam energy interacting with the material and the distance between the two windows.

In Fig. 5.22, shows the beam scattering angle with respect to the beam kinetic energy and distance traveled in air using Eq. (5.15). The radiation length of air is 36.62 g/cm^2. The beam kinetic energy is varied from 0 to 66 MeV, the maximum beam energy attainable at Crocker Nuclear Laboratory, and the length of air traversed was varied from 0 to 2 cm.

At 10 MeV kinetic energy, with a gap of air of 1 cm, the scattering angle is 0.1 radians, and with a gap of 0.5 cm the scattering is reduced to 0.06 radians. In Fig. 5.23, demonstrates the scattering angle from eq.(5.15) at beam energies from 0 to 100 MeV with a fixed target of Titanium with a length of 0.127 mm and a Kapton target of length 0.3 mm.

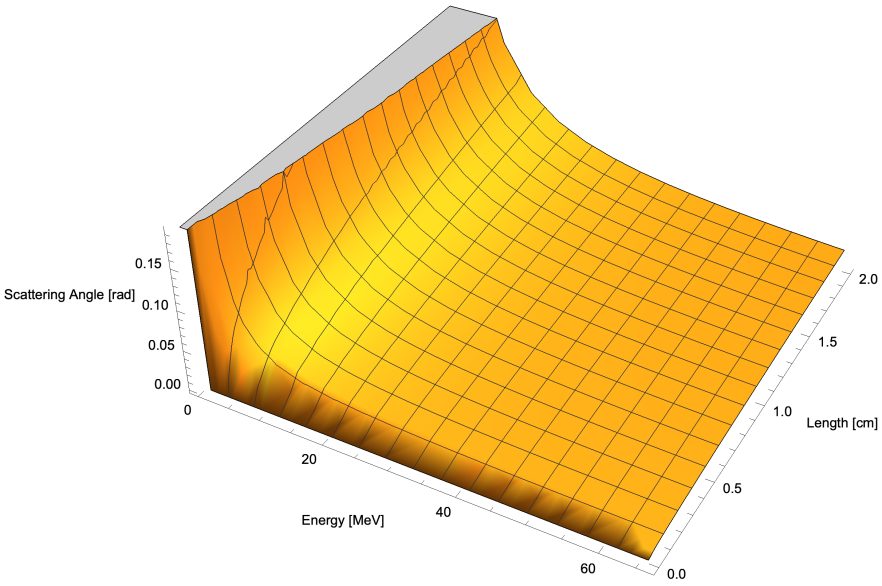

Figure 5.22: Beam Scattering Due to Air with varying Beam Kinetic Energy and distance traveled in the matter

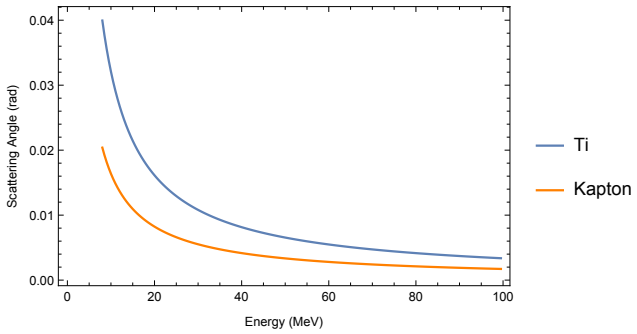

Figure 5.23: Beam Scattering angle at fixed target thickness for Titanium (Blue) and Kapton (Orange) with varying beam energies.

Since the targets are at fixed lengths, using the mean energy loss per distance traveled $< dE/dx >$ from NIST PSTAR tables, the energy loss can be calculated from initial beam energy. This is demonstrated in Fig. 5.24. With initial kinetic energy of 9 MeV and assuming energy loss through the air is $\Delta E \ll 1$ for a small gap, the energy loss through Kapton is $\Delta E \approx 2.14$ MeV, then an additional $\Delta E \approx 2.62$ MeV through the titanium window. The final beam energy would be ≈4.24 MeV. At initial kinetic energy of 10 MeV, the finial beam kinetic energy would be 5.84 MeV.

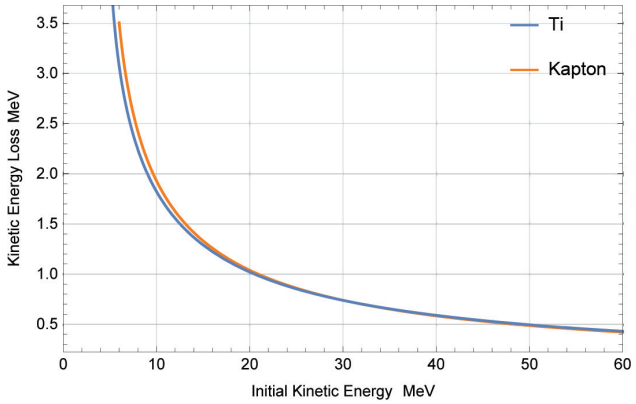

Figure 5.24: Beam Energy Loss at fixed target thickness for Titanium (Blue) and Kapton (Orange) with varying beam energies.

5.8.1.1 G4Beamline Simulations

For G4Beamline simulations [52], an initial beam distribution of $\sigma_{x,y} = 3$ mm and $\sigma_{x',y'} = 2$ mrad. The beam distribution is placed 2 mm before hitting a Kapton target of 0.3 mm thickness. The simulation also includes a varying air gap, followed by a Titanium window of thickness of 0.127 mm. A virtual detector is placed 106.425 mm away from the Ti window. This corresponds to the center of the gas sheet beam profile monitor. The initial beam kinetic energy was 10 MeV and a gap of air of 5 cm.

The beam distribution at the center of the gas sheet beam profile monitor is $\sigma_x = 8.42$ mm and $\sigma_y = 7.13$ mm. The transverse distribution is shown in Fig. 5.25. The average beam energy is reduced to 5.78 MeV.

With increased energy initial energy of 20 MeV, the RMS transverse beam distribution reduces down to $\sigma_x = 5.83$ mm and $\sigma_y = 5.70$ mm. The beam energy is reduced to 17.84 MeV at the interaction region. With a gap of air of 1 cm, to achieve a beam energy in the interaction chamber of 2.5 MeV, the initial beam energy from the cyclotron would need to be less than 10 MeV.

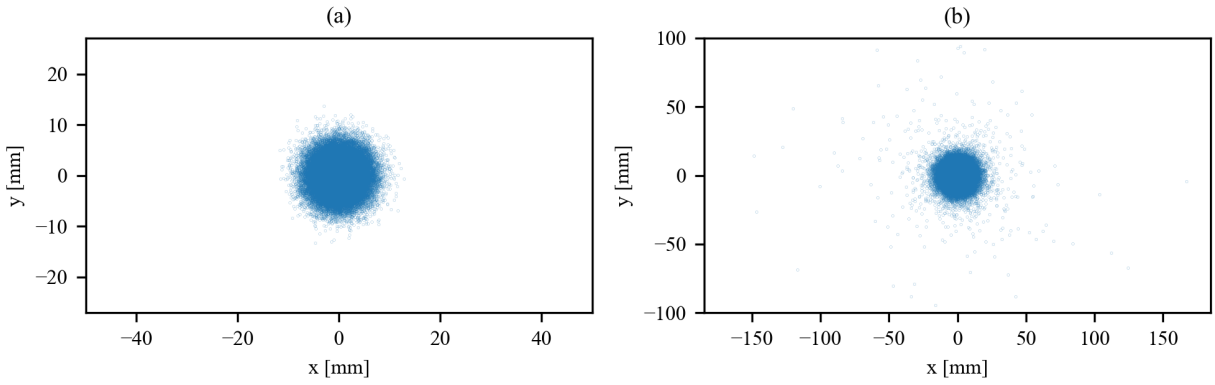

Figure 5.25: (a) Initial beam transverse distribution and (b) at the center of gas sheet beam profile monitor.

5.8.1.2 WARP Simulations

Due to expected space charge effects in IOTA, simulations of beam-gas interactions have been performed using Warp [53]. Warp models ionization process and space charge effects, as well as the electrode strength for ion extraction. However, to quantify expected results at Crocker Nuclear Laboratory, their beam parameters will be used. It is to note that since the beam current is up to 0.100μA, space charge effects are not predominant like IOTA's 8 mA of beam current.

A Gaussian distribution beam $\sigma_{x,y} = 3.5$ mm was injected, with the gas sheet thickness of 0.6 mm, rotated by 45deg with respect to the z-axis. The electrode stack from Section 5.6 was also placed. Figure 5.26 shows the simulation setup.

The distribution of ions was recorded at a y-slice greater than 4 cm over the course of the beam pulse of 1.77 μs. The horizontal distribution of the beam should match the horizontal distribution of the ions. Whereas the vertical distribution of the beam should match the longitudinal position of the ions. The horizontal and vertical distribution of the beam is

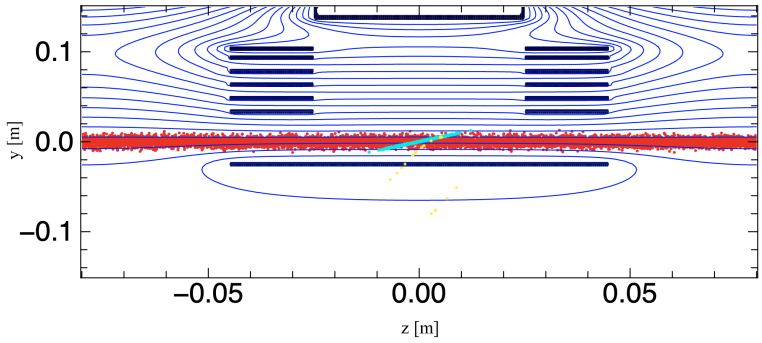

Figure 5.26: WARP simulation domain in the y-z plane. Shown are the ion macroparticles (cyan) and electrons (yellow) generated by the beam (red) interacting with the gas (not shown). The cross section of the electrodes is outlined in black, with the top plate being the microchannel plate, with its potential field lines in blue. This snap show was recorded 183.06 ns into the simulation.

shown in Fig. 5.27 with bin size of 0.25 mm. The horizontal and longitudinal distribution of all ions that passed through $y \geq 4.0$ cm is shown in Fig. 5.28.

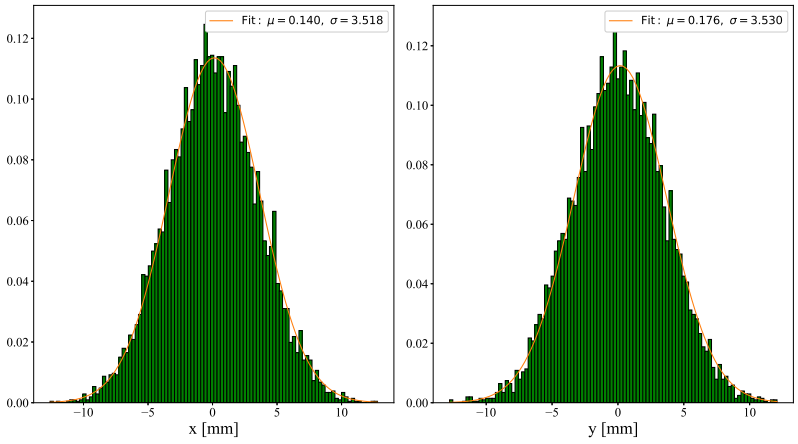

Figure 5.27: Transverse distribution for the beam ($x-$left, $y-$right), with Gaussian fits.

The vertical RMS distribution is in agreement to within 1%, whereas in horizontal it is 7%. This can attribute to a non-perfect uniform vertical electric field. As this could have a slight focusing or defocusing effect on the ions, depending on the radial component of the electric field.

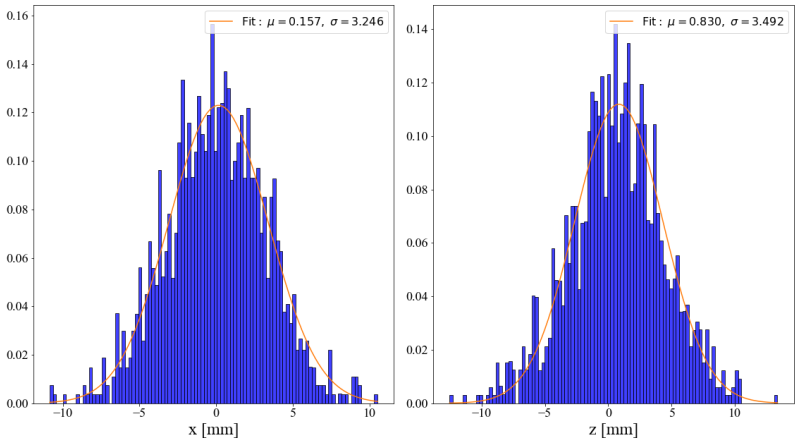

Figure 5.28: Transverse distribution ($x-$left, $z-$right) for all ions to have passed through $y = 4.0$ cm, with Gaussian fits.

5.9 Development and Commissioning Outlook

The gas sheet beam profile monitor (GSBPM) next step is to measure the transverse profile of Crocker Nuclear Laboratory proton beam. These measurements will give insight on operational procedures using the GSBPM, as well as any modification needed to run in the Integrable Optics Test Accelerator (IOTA). In IOTA beamline design, correct magnets would need to be placed up and downstream of the GSBPM to compensate for the deflection of the beam produced by the electrode stack. Necessary differential pumping would be needed to ensure the vacuum quality throughout the rest of the ring would need to be added as well. To fit the design requirements of IOTA constraints a new interaction chamber was designed as seen in Fig. 5.29. The design has three turbomolecular pumps to ensure ultra-high vacuum requirements throughout the ring.

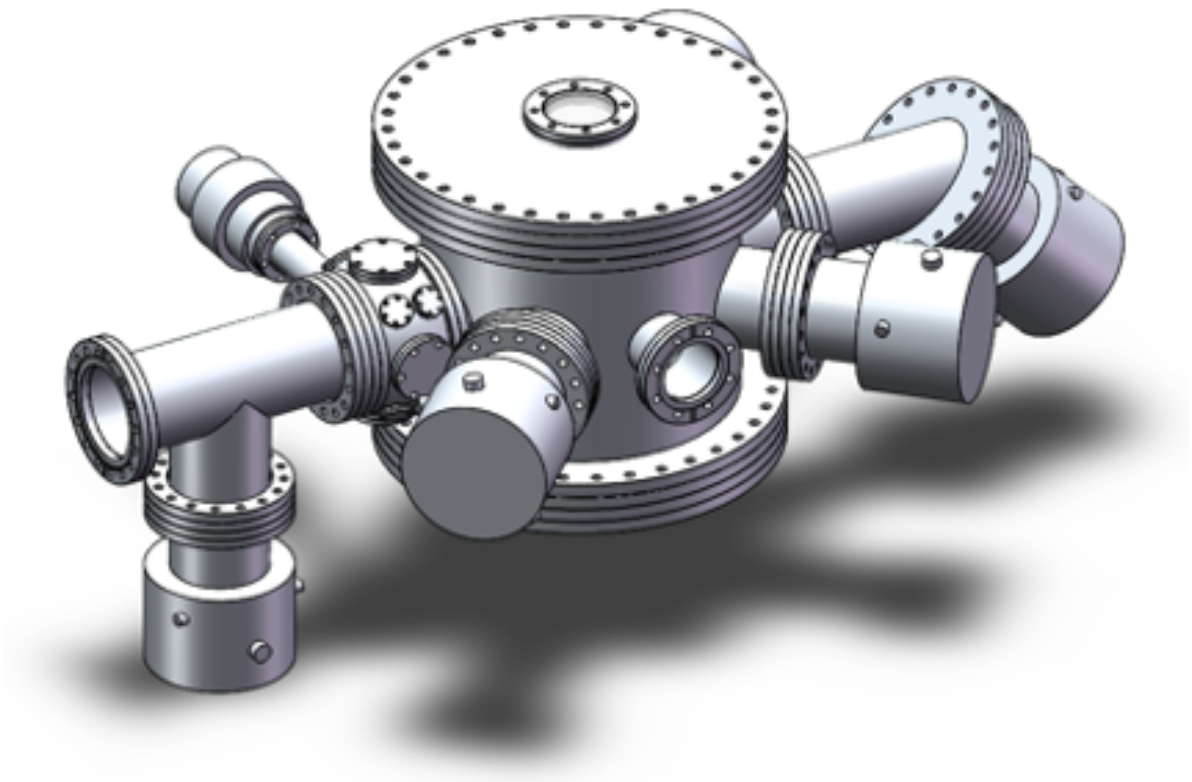

Figure 5.29: GSBPM chamber for use in IOTA.

CHAPTER 6

CONCLUSION

This work presented in this dissertation describes nonlinear beam dynamics in the Integrable Optics Test Accelerator and experimental results. Although simulations of beam dynamics in the Integrable Optics Test Accelerator has been done in the past, experimental verification is needed to confirm the theory. The beam instrumentation used to collect data was beam position monitors, synchrotron light monitors, and direct current current transformer. Analysis of tune measurements was taking Fast Fourier transform from the beam position monitors. Resonance stability, as well as, the beam splitting was observed with the direct current current transformer and synchrotron light monitors. In which the beam was demonstrated to survive on integer resonance and crossing over other higher order resonances. Additionally, higher nonlinear strength of beam splitting was investigated. The application for split beams can further be explored, e.g., beam extraction. However, numerical tracking simulation has not been implemented yet. The Danilov-Nagaitsev nonlinear magnet also demonstrated to have a large tune spread of $\Delta Q_y = 0.125 \pm 0.0016$ at $t = 0.49$. Allowing for stability in space charge tune shifts in high intensity proton beams.

The development of a gas sheet beam profile monitor for use in proton transverse beam diagnostic was also discussed. The discussion of the instrumentation device was broken down into three main categories: gas injection, extraction, and readout. The prospect of testing in a future proton beam-line was also discussed. For the gas injection system, background and simulation is presented. This was to ensure to have a gas sheet with proper resolution and not to degrade a beam lifetime. An apparatus at Fermilab was built to measure the gas distribution from the injection system. The extraction system was also developed with

simulation. To prepare for testing the gas sheet beam profile monitor at the Crocker Nuclear Laboratory, simulations were done to determine the condition of the expected signal as the two vacuum systems were separated. Since the wanted beam condition for a one-shot measurement is needed to be similar to IOTA turn-by-turn operation. Outlook, further development, and beam testing are contingent on the outlook of the current global pandemic [54].

REFERENCES

1. Courant, E. D. & Snyder, H. S. Theory of the alternating-gradient synchrotron. *Annals of Physics* **3,** 1–48 (1958).
2. Wiedemann, H. *Particle accelerator physics: Third edition* 1–948 (Springer Berlin Heidelberg, 2007).
3. Antipov, S. *et al.* IOTA (Integrable Optics Test Accelerator): facility and experimental beam physics program. *Journal of Instrumentation* **12,** T03002–T03002 (Mar. 2017).
4. Danilov, V. & Nagaitsev, S. Nonlinear accelerator lattices with one and two analytic invariants. *Phys. Rev. ST Accel. Beams* **13,** 84002 (Aug. 2010).
5. Eldred, J., Lebedev, V. & Valishev, A. Rapid-cycling synchrotron for multi-megawatt proton facility at Fermilab. *Journal of Instrumentation* **14,** P07021–P07021 (July 2019).
6. Webb, S. D. *et al. Suppressing Transverse Beam Halo with Nonlinear Magnetic Fields* in *Proc. 4th International Particle Accelerator Conference (IPAC'13), Shanghai, China, 12-17 May 2013* (2013).
7. Lee, S. Y. *Accelerator Physics, 3rd ed.* 1–533 (World Scientific Publishing Co., Jan. 2011).
8. Weihreter, E. *Compact superconducting synchrotron radiation sources* in *CAS - CERN Accelerator School and Daresbury Laboratory : Course on Synchrotron Radiation and Free-electron Lasers* (CERN, Chester, UK, Apr. 1990), 429.
9. Jackson, J. D. *Classical Electrodynamics; 3rd ed.* (Wiley, New York, NY, 1999).
10. Freemire, B. T. *Private Communication* Feb. 2018.

11. Reiser, M. *Theory and design of charged particle beams; 2nd ed.* (Wiley, 2008).

12. Holmes, J. A., Danilov, V. V., Galambos, J. D., Jeon, D. & Olsen, D. K. Space charge dynamics in high intensity rings. *Phys. Rev. ST Accel. Beams* **2,** 114202 (Nov. 1999).

13. Nagaitsev, S., Valishev, A. & Danilov, V. *Nonlinear optics as a path to high-intensity circular machines* in *HB 2010 - 46th ICFA Advanced Beam Dynamics Workshop on High-Intensity and High-Brightness Hadron Beams* (Morschach, Switzerland, 2010), 676–680.

14. Mitchell, C. E., Ryne, R. D. & Hwang, K. Bifurcation analysis of nonlinear Hamiltonian dynamics in the Fermilab Integrable Optics Test Accelerator. *Physical Review Accelerators and Beams* **23,** 064002 (June 2020).

15. Wolfram Research, I. *Mathematica, Version 11.3*

16. Shiltsev, V. Improvement Plans of Fermilab's Proton Accelerator Complex. *Journal of Physics: Conference Series* **888,** 12043 (Sept. 2017).

17. Eddy, N. *et al. Beam Instrumentation at the Fermilab IOTA Ring* in *Proc. IBIC'19* (JACoW Publishing, Geneva, Switzerland, Nov. 2019), 22–28.

18. Antipov, S. A., Didenko, A., Lebedev, V. A. & Valishev, A. *Stripline Kicker for Integrable Optics Test Accelerator* in *Proc. 6th International Particle Accelerator Conference (IPAC'15), Richmond, VA, USA, May 3-8, 2015* (JACoW, Geneva, Switzerland, June 2015), 3390–3392.

19. Kuklev, N., Kim, Y. K. & Romanov, A. L. *Synchrotron Radiation Beam Diagnostics for the Integrable Optics Test Accelerator* in *Proc. 9th International Particle Accelerator Conference (IPAC'18), Vancouver, BC, Canada, April 29-May 4, 2018* (JACoW Publishing, Geneva, Switzerland, June 2018), 2073–2076.

20. Grote, H. & Schmidt, F. *Mad-X - an upgrade from mad8* in *Proceedings of the 2003 Particle Accelerator Conference* **5** (May 2003), 3497–3499.

21. McNevin, J. D., Agustsson, R. B. & O'Shea, F. H. *Mechanical Design and Manufacturing of a Two Meter Precision Non-Linear Magnet System* in *Proc. of North American Particle Accelerator Conference (NAPAC'16), Chicago, IL, USA, October 9-14, 2016* (JACoW, Geneva, Switzerland, Jan. 2016), 578–581.

22. DiMarco, J. & Krzywinski, J. *MTF Single Stretched Wire System* tech. rep. (Fermi National Accelerator Laboratory, 1996).

23. Prebys, E., Antipov, S. A., Carlson, K., Piekarz, H. & Valishev, A. *Proton Injection into the Fermilab Integrable Optics Test Accelerator (IOTA)* in *Proc. of International Particle Accelerator Conference (IPAC'16), Busan, Korea, May 8-13, 2016* (JACoW, Geneva, Switzerland, June 2016), 1638–1640.

24. Castaneda, C. M. *Crocker Nuclear Laboratory (CNL) radiation effects measurement and test facility* in *2001 IEEE Radiation Effects Data Workshop. NSREC 2001. Workshop Record. Held in conjunction with IEEE Nuclear and Space Radiation Effects Conference (Cat. No.01TH8588)* (2001), 77–81.

25. Romanov, A. & et al. *Recent Results and Opportunities at the IOTA Facility* in *North American Particle Accelerator Conf. (NAPAC'19)* (Lansing, MI, USA, 2019), WEXBA2.

26. Piot, P. & Halavanau, A. *A High-Level Python Interface to the Fermilab ACNET Control System* in *Proc. of North American Particle Accelerator Conference (NAPAC'16), Chicago, IL, USA, October 9-14, 2016* (JACoW, Geneva, Switzerland, 2017), 383–386.

27. Kuklev, N. *pyIOTA (https://github.com/nikitakuklev/pyIOTA)* 2020.

28. Hall, C. C. *et al. First Measurements of Nonlinear Decoherence in the IOTA Ring* in *Proc. 10th International Particle Accelerator Conference (IPAC'19), Melbourne, Australia, 19-24 May 2019* (JACoW Publishing, Geneva, Switzerland, 2019), 3286–3288.

29. Szustkowski, S., Chattopadhyay, S., Kuklev, N., Romanov, A. & Valishev, A. *Nonlinear Tune-Shift Measurements in the Integrable Optics Test Accelerator* in *Proc. of North American Particle Accelerator Conference (NAPAC'19), Lansing, MI, USA, September 1-6, 2019* (2019).

30. Darboux, G. Sur un problème de mécanique. *Arch. Néerlandaises Sci* **6,** 371 (1901).

31. Roth, A. in *Vacuum Technology (Third Edition)* (ed Roth, A.) Third Edit, 17–61 (Elsevier, Amsterdam, 1990).

32. Lafferty, J. M. *Foundations of vacuum science and technology* (Wiley New York, 1998).

33. Clausing, P. Über die Strahlformung bei der Molekularströmung. *Zeitschrift für Physik* **66,** 471–476 (1930).

34. Clausing, P. The Flow of Highly Rarefied Gases through Tubes of Arbitrary Length. *Journal of Vacuum Science and Technology* **8,** 636–646 (Sept. 1971).

35. Dayton, B. B. *Gas Flow Patterns at Entrance and Exit of Cylindrical Tubes.* in *Trans. 3rd. Natl. Vac. Symp.* (1956), 5–11.

36. Cole, R. J. in *Rarefied Gas Dynamics, Parts I and II* 261–272 (1976).

37. Giordmaine, J. A. & Wang, T. C. Molecular Beam Formation by Long Parallel Tubes. *Journal of Applied Physics* **31,** 463–471 (1960).

38. Clausing, P. Stationary Flow of Very Dilute Gases. *Physica* **9,** 65–80 (1929).

39. Vályi, L. *Atom and Ion Sources* (Wiley, New York, NY, 1977).

40. Lowry, R. A. & Miller, G. H. Ionization Yield of Protons in Nitrogen and Argon. *Phys. Rev.* **109,** 826–831 (Feb. 1958).

41. Bakker, C. J. & Segrè, E. Stopping Power and Energy Loss for Ion Pair Production for 340-Mev Protons. *Phys. Rev.* **81,** 489–492 (Feb. 1951).

42. Larson, H. V. Energy Loss Per Ion Pair for Protons in Various Gases. *Phys. Rev.* **112,** 1927–1928 (Dec. 1958).

43. Zyla, P. A. *et al.* Review of Particle Physics. *Progress of Theoretical and Experimental Physics* **2020** (Aug. 2020).

44. Berger, M. J., Coursey, J. S., Zucker, M. A., Chang, J., *et al. Stopping-power and range tables for electrons, protons, and helium ions* (NIST Physics Laboratory Gaithersburg, MD, 1998).

45. Szustkowski, S., Chattopadhyay, S., Crawford, D. J. & Freemire, B. T. *Development of a Gas Sheet Beam Profile Monitor for IOTA* in *Proc. 9th International Particle Accelerator Conference (IPAC'18), Vancouver, BC, Canada, April 29-May 4, 2018* (JACoW Publishing, Geneva, Switzerland, June 2018), 2326–2329.

46. Ogiwara, N. *et al. A Non-destructive Profile Monitor Using a Gas Sheet* in *Proc. of International Particle Accelerator Conference (IPAC'16), Busan, Korea, May 8-13, 2016* (JACoW, Geneva, Switzerland, June 2016), 2102–2104.

47. Kersevan, R. & Ady, M. *Recent Developments of Monte-Carlo Codes Molflow+ and Synrad+* in *Proc. 10th International Particle Accelerator Conference (IPAC'19), Melbourne, Australia, 19-24 May 2019* (JACoW Publishing, Geneva, Switzerland, June 2019), 1327–1330.

48. Szustkowski, S., Chattopadhyay, S., Crawford, D. J. & Freemire, B. T. *Gas Jet Profile Monitor for Use in IOTA Proton Beam* in *Proc. of International Beam Instrumentation Conference (IBIC'17), Grand Rapids, MI, USA, 20-24 August 2017* (JACoW, Geneva, Switzerland, Mar. 2017), 347–349.

49. Szustkowski, S., Chattopadhyay, S., Crawford, D. J. & Freemire, B. T. *Skimmer-Nozzle Configuration Measurements for a Gas Sheet Beam Profile Monitor* in *Proc. of North American Particle Accelerator Conference (NAPAC'19), Lansing, MI, USA, September 1-6, 2019* (2019).

50. Halbach, K. & Holsinger, R. F. Superfish -A computer program for evaluation of RF cavities with cylindrical symmetry. *Part. Accel.* **7,** 213–222 (1976).

51. Putignano, M., Kühnel, K. U., Schröter, C. D. & Welsch, C. P. A fast, low perturbation ionization beam profile monitor based on a gas-jet curtain for the ultra low energy storage ring. *Hyperfine Interactions* **194,** 189–193 (Nov. 2009).

52. Roberts, T. J. & Kaplan, D. M. *G4beamline simulation program for matter-dominated beamlines* in *2007 IEEE Particle Accelerator Conference (PAC)* (June 2007), 3468–3470.

53. Friedman, A. *et al.* Computational Methods in the Warp Code Framework for Kinetic Simulations of Particle Beams and Plasmas. *IEEE Transactions on Plasma Science* **42,** 1321–1334 (2014).

54. Cucinotta, D. & Vanelli, M. WHO Declares COVID-19 a Pandemic. *Acta bio-medica : Atenei Parmensis* **91,** 157–160 (Mar. 2020).